COMPUTER METHODS IN APPLIED MECHANICS AND ENGINEERING
doi:10.1016/j.cma.2014.11.027

Explicit dynamics simulation of blade cutting of thin elastoplastic shells using "directional" cohesive elements in solid-shell finite element models

Mara Pagani[a], Umberto Perego[b,*]

[a] *Comsol S.r.l., v.le Duca degli Abruzzi 103, 25124 Brescia, Italy*
[b] *Department of Structural Engineering, Politecnico di Milano, Piazza L. da Vinci,32, 20133 Milan, Italy*

Abstract

The intentional or accidental cutting of thin shell structures by means of a sharp object is of interest in many engineering applications. The process of cutting involves several types of nonlinearities, such as large deformations, contact, crack propagation and, in the case of laminated shells, delamination. In addition to these, a special difficulty is represented by the blade sharpness, whose accurate geometric resolution would require meshes with characteristic size of the order of the blade curvature radius. A computational finite element approach for the simulation of blade cutting of thin shells is proposed and discussed. The approach is developed in an explicit dynamics framework. Solid-shell elements are used for the discretization, in view of possible future inclusion in the model of delamination processes. Since a sharp blade can interfere with the transmission of cohesive forces between the crack flanks in the cohesive process zone, standard cohesive interface elements are not suited for the simulation of this type of problems unless extremely fine meshes, with characteristic size comparable to the blade curvature radius, are used. To circumvent the problem, the use of a new type of directional cohesive interface element, previously proposed for the simulation of crack propagation in elastic shells, is further developed and reformulated for application to the cutting of elastoplastic thin structures, discretized by solid-shell elements. The proposed approach is validated by means of application to several cutting problems of engineering interest.

Keywords: blade cutting, explicit dynamics, solid-shell elements, cohesive model, crack propagation.

1. Introduction

In real life there are many situations in which thin shells (plates, foils, sheets, membranes, tissues, ...) are cut by sharp objects (blades, wedges, splinters, ...). In many cases the cut is intentional, as

* Corresponding author
Email addresses: mara.pagani@comsol.com (Mara Pagani), umberto.perego@polimi.it (Umberto Perego)

e.g. in military applications, in manufacturing processes, in surgery, in package opening, and so on. In other cases the cutting is due to an accident, as e.g. in the case of ship grounding, collisions or explosions. In all cases, the process of cutting is a complicated mechanical process involving several types of nonlinearities: large strains, inelastic deformation, fracture propagation and contact. In the case of the cutting of laminated shells, delamination has also to be accounted for.

Early experiments on cutting processes of thin metal plates date back to the beginning of the eighties, mainly in the naval engineering field, to provide insights into the problem of ship grounding, whereby a ship hull is cut by a sharp rock. These tests were mainly performed dynamically in a drop-hammer rig with a cutting wedge (see e.g. Jones and Jouri, 1987). The main dissipation mechanisms were identified as plastic bending of the folding lateral flaps, fracture energy and friction, leading to empirical formulas for the work of cutting. Quasi-static tests on the wedge cutting of metal plates were conducted by Lu and Calladine (1990). On the basis of these tests, the authors proposed a single-term empirical formula for the work of cutting, where the yield limit was the only material parameter playing a role. Atkins (1990, 1991), suggested that far-field (plastic bending) events and near-tip (fracture) events, where the blade edge interacts with the fracture process zone, should give rise to separate, independent terms in the expressions for the energy absorption and the indentation force. Wierzbicki and Thomas (1993) showed that the far-field and the near-tip deformation mechanisms can be related by the rolling radius of the cylindrical flaps formed in the wake of the cut. They developed a simple kinematic model describing the main features of the cutting process. For the same type of problem, Zheng and Wierzbicki (1996) derived an analytical formula to predict the wedge cutting force. Other valuable contributions are contained in the works by Simonsen and Wierzbicki (1998) and Muscat-Fenech and Atkins (1998). It is also worth mentioning the recent monograph on this subject by Atkins (2009).

From the point of view of the simulation, the problem is dominated by the existence of two small geometric scales. The first one is the scale of the thickness of the thin-walled structure, which is usually orders of magnitude smaller than the in plane global dimensions. The second small scale is determined by the curvature radius of the cutting blade, which can be of the order of microns, or even less, in the case of a sharp blade. While the first scale is usually resolved using shell elements, the resolution of the second scale would require extremely fine meshes, unacceptable in terms of computational costs, and therefore requires special provisions.

In view of the high nonlinearity of the problem, the finite element simulation of cutting is often better dealt with in an explicit dynamics framework. In commercial codes, such as Abaqus or LS-Dyna, this type of simulations can be usually attacked using the element deletion method, whereby the element is eliminated from the mesh when the fracture criterion is satisfied at that element (see e.g. AbuBakar and Dow, 2013, for a recent application to the simulation of ship grounding). Although with this technique

the simulation can be easily carried out and good results can be obtained for the simulation of diffused damage due to explosions or crashing against large obstacles, it is difficult to justify the element deletion from a physical point of view, even though recent contributions (see e.g. Pandolfi and Ortiz, 2012) seem to provide a more rigorous framework under this respect. Furthermore, the result may be strongly affected by the element size with respect to other geometric characteristics, such as the blade curvature radius.

Another approach consists of introducing the crack discontinuity in the finite element displacement model. This can be done by either enriching the displacement field, as e.g. in the extended finite element method (XFEM, see e.g. Moës et al., 1999), or by allowing a crack to propagate along element edges, by duplicating nodes (see e.g. Li and Siegmund, 2002; Cirak et al., 2005; Zavattieri, 2006): when the fracture criterion is satisfied at a node, the node is duplicated and the adjacent elements can separate along the previously common edge. One argument in favor of the node separation method in cutting problems is that the main crack propagation direction is dictated by the imposed blade movement, so that the mesh can be a priori adjusted to follow the correct propagation path, without the need to use extremely refined meshes. Explicitly introducing a displacement discontinuity in the model is in general more difficult to implement than the element deletion method, however, the physical meaning is clear and therefore the latter approach is preferred in the present contribution.

A fundamental ingredient in the simulation of blade cutting of thin sheets is the capability to simulate crack propagation in shells. Apart from the early contributions of Rice and Levy (1972) and Lee and Parks (1998), simulations based on the explicit consideration of a displacement discontinuity have started to be proposed only recently. Li and Siegmund (2002) formulated a cohesive interface element for the simulation of crack growth in thin metal sheets which can be applied to shell element meshes of the finite element code Abaqus. Cirak et al. (2005) considered Kirchhoff-Love conforming shell elements and inserted cohesive interfaces between element edges, referring to the crack average surface for the definition of the normal to the opening crack. Zavattieri (2006) proposed an interface cohesive element to be placed between Belytschko-Lin-Tsay shell elements (Belytschko et al., 1984), whereby the damage contribution due to the bending moment transmitted across the interface is explicitly taken into account. Areias and Belytschko (2005) formulated a Mindlin-Reissner type shell element for fracture analysis based on XFEM, while Areias et al. (2006) considered a Kirchhoff-Love quadrilateral shell element for arbitrary crack propagation that employs large rotations about moving axes using a reinterpretation of the XFEM methodology. Song and Belytschko (2009) developed an XFEM approach based on the four node Belytschko-Lin-Tsay element, endowed with a nonlocal strain-based fracture criterion. Larsson et al. (2011) modeled through-the-thickness crack propagation in thin walled structures using 7-parameters triangular shell elements with extensible director and XFEM. A rate dependent cohesive zone model was used to limit crack speed. The model has been recently refined in Mostofizadeh et al. (2013),

where special consideration has been given to limiting stress oscillations produced by elementwise description of crack propagation, implementing smoothed nodal correction forces, as originally proposed by Menouillard and Belytschko (2010). Ahmed et al. (2012) considered crack propagation in solid-shell elements. The discontinuity is introduced through the element implementing a modified XFEM approach based on the overlapping element technique of Hansbo and Hansbo (2004). Worth mentioning are also the meshless approaches to crack propagation in shells recently proposed in Caleyron et al. (2012) and in Ren and Li (2012).

With the exception of the work by Ahmed et al. (2012), in which fracture propagation in solid-shell elements is considered, the other contributions consider classical shell elements of various types. Solid-shell elements are elements with displacement degrees of freedom only (see e.g. Hauptmann and Schweizerhof, 1998). They allow for a straightforward incorporation of complex 3D material models, are easy to use in combination with 3D solid elements, offer good accuracy in the through-the thickness stress distribution, a necessary requisite in view of possible future consideration of delamination processes due to cutting, and for this reason they are employed also in this work. Solid-shell elements have been predominantly used in the framework of implicit formulations and exhibit some features which may lead to an increase of computational costs when implemented in an explicit dynamics code. Solid-shell elements are known to suffer locking problems, such as shear locking, which is typically cured by the ANS (Assumed Natural Strain) method, and volumetric locking, which is usually controlled by means of the EAS (Enhanced Assumed Strain) method. In this work, reference is made to the solid-shell formulation recently presented by Schwarze and Reese (2011), where this techniques have been successfully implemented. The EAS method, requiring at each time step the implicit solution of a nonlinear problem for the computation of the enhanced variables, is particularly expensive in terms of computational effort when used in explicit dynamics. To reduce computational costs, explicit update of the enhanced variables has been proposed in Pagani et al. (2013) and has also been used in this work. An additional problem is represented by the fact that solid-shell elements have a thickness, which is significantly smaller that the other two dimensions. This leads to a high finite element maximum eigenfrequency and, consequently, to a very small stable time step. In the present work the selective mass scaling technique proposed in Cocchetti et al. (2012) has been applied to increase the stable time step without affecting the dynamical response, while the approach proposed in Pagani et al. (2013) has been used for the estimate of the critical time-step size and for the optimal choice of the mass scaling factor.

When a displacement discontinuity is introduced in the model to simulate the propagating crack, in most cases an interface cohesive element is interposed between the separating crack flanks to account for the progressive release of fracture energy. A cohesive fracture modeling can be pursued without special difficulty in combination with both an XFEM treatment of the displacement discontinuity (see

e.g. Moës and Belytschko, 2002; Mariani and Perego, 2003) and with cracks propagating along element edges (see e.g. Cirak et al., 2005). In cutting problems, the crack flanks can undergo large opening displacements also in proximity of the crack tip, depending on the shape of the cutting tool. In the presence of ductile materials, it may be necessary to consider the configuration change in the definition of the cohesive traction. Fagerström and Larsson (2006) proposed to account for the contribution of the cohesive traction making reference to one of the two flanks and enforcing the cohesive constitutive behavior in terms of the Mandel stress vector. Wells et al. (2002) and Cirak et al. (2005) proposed to define a reference surface as the average surface between the separating crack flanks and to refer the cohesive normal and tangential traction components, needed to enforce the interface behavior, to this surface. Giampieri and Perego (2011) formulated a cohesive interface element to model the localized deformation developing in the folding process of thin sheets. As in Cirak et al. (2005), they defined a reference average interface. To avoid the effect of rigid rotations when considering interface deformation starting from an opened configuration, they defined a rotation-free interface "strain", different from the displacement jump. Adopting a dual, static point of view, Vossen et al. (2013) noted that rotational equilibrium of an opened cohesive crack is only possible when the traction vector is aligned with the crack opening vector.

In the case of blade cutting, when the cutting tool is sharp and the material ductile, it may happen that the blade interacts with the material in the process zone. In classical cohesive interfaces, cohesive forces are typically transmitted along a straight line connecting the separating crack sides. In the case that the ultimate cohesive opening displacement is of a magnitude comparable to the blade curvature radius, the presence of the blade can interfere with the correct transmission of the cohesive forces. To circumvent this problem and to account for these possible interactions, a new type of cohesive interface element, to be interposed between adjacent separating solid-shell elements, the so-called "directional" cohesive element, is considered in this work, in the line of what proposed in Frangi et al. (2010) in an elastic-brittle context, in combination with classical quadrilateral shell elements.

In the present paper a computational strategy for the simulation of blade cutting of thin-walled elasto-plastic structures is presented and validated by means of numerical tests. Solid-shell finite elements of the type presented in Schwarze and Reese (2011) have been implemented in an explicit dynamics, large strains, elastoplastic, in-house finite element code, together with the modifications proposed in Pagani et al. (2013) and the selective mass scaling technique proposed by Cocchetti et al. (2012). Crack propagation is accounted for by introducing cohesive interfaces between separating element edges, whenever a suitable crack propagation criterion is met. The "directional" cohesive element approach proposed in Frangi et al. (2010) has been adopted to account for the interaction between the blade and the cohesive process zone. Even though the basic idea of the directional cohesive elements has been here used in

the original form presented in Frangi et al. (2010), its use in conjunction with solid-shell elastoplastic elements, which is considered in the present paper, requires a substantially new implementation, together with the definition of initiation and propagation criteria suitable for elastoplastic materials.

2. Directional cohesive element concept

2.1. Problem formulation

In classical cohesive elements, cohesive forces are typically transmitted in a direction determined by the direction of the displacement jump and by the cohesive law, which may require to distinguish between traction normal and tangential components. When the fracture of a very ductile material is the consequence of the action of a sharp object, it may happen that the blade intersects the line of action of the cohesive forces, leading to inaccurate simulations with unrealistic effects. The problem is due to the fact that, according to the cohesive zone idealization, the three-dimensional process zone developing at the mesoscale (i.e. the scale of the shell thickness) is collapsed onto a bi-dimensional interface. When the interface opens due to crack propagation and the opening is infinitesimal, the volume of the region delimited by the separating crack flanks is also infinitesimal. On the other hand, when the cohesive interface opening is large, the region delimited by the separating crack flanks occupies a finite volume, which in certain cases can be crossed by the cutting blade (Figure 1a). The obvious remedy would be to adopt a discretization capable to resolve the blade radius of curvature (Figure 1b) and to account for the actual complex interaction between the cutting blade and the shell material within the cohesive process zone. However, if the blade is sharp, this could lead to prohibitive computational costs. To circumvent this problem and to account for these possible interactions, a new type of cohesive interface element, the so-called "directional" cohesive element, to be interposed between adjacent separating finite elements, has been proposed in Frangi et al. (2010) in conjunction with elastic quadrilateral shell elements of the MITC4 type (Bathe and Dvorkin, 1985). The same technique is adopted also in the present work in conjunction with eight-node, reduced integration solid-shell elements with hourglass control of the type proposed by Schwarze and Reese (2011). The large strain elastoplastic behavior of the bulk material has been modeled according to the unified hyperelastic-plastic approach proposed by Simo and Miehe (1992), based on a multiplicative decomposition of the deformation gradient.

Consider a shell body with initial configuration $\mathcal{B}_0$ occupying the volume Ω_0 with boundary $\partial\Omega_0$. The body undergoes a motion described by a deformation mapping $\boldsymbol{\chi}(\mathbf{X}, t)$, $t \in [0, T]$. Let $\mathbb{F}$ be the deformation gradient, $\mathbb{E}$ the Green Lagrange strain tensor and $\mathbb{S}$ the second Piola-Kirchhoff stress tensor. Let Ω be the volume occupied by the body in the deformed configuration $\mathcal{B}$.

Assume the existence of a cohesive crack through the thickness of the shell body. When the crack is closed it is identified by a zero thickness interface $\bar{\Gamma}_C$ in the original configuration, which transforms

into Γ_C as a consequence of the deformation process. When the crack opens, geometric discontinuities $\boldsymbol{\delta} = \mathbf{x}^+ - \mathbf{x}^-$ occur across the reference interface Γ_C, where $\mathbf{x}^+$ and $\mathbf{x}^-$ denote the positions of material points belonging to the two separating flanks of the crack in the current configuration, denoted as Γ_C^+ and Γ_C^- (Figure 2). For dynamic problems in the absence of damping, the variational balance equation can be written as

$$\delta\Pi_{\text{kin}} + \delta\Pi_{\text{int}} - \delta\Pi_{\text{ext}} = 0 \tag{1}$$

$\delta\Pi_{\text{kin}}$, $\delta\Pi_{\text{int}}$ and $\delta\Pi_{\text{ext}}$ being the kinetic, internal and external work, respectively. The kinetic term assumes the usual expression

$$\delta\Pi_{\text{kin}} = \int_\Omega \rho\ddot{\mathbf{u}} \cdot \delta\mathbf{u}\, \mathrm{d}\Omega \tag{2}$$

ρ being the mass density of the material, $\mathbf{u}$ the vector of nodal displacements and $\ddot{\mathbf{u}}$ the vector of nodal accelerations. In the presence of a body with a propagating cohesive fracture, the bulk material and the cohesive interface provide two separate contributions to the internal virtual work:

$$\delta\Pi_{\text{int}} = \delta\Pi_{\text{S,int}} + \delta\Pi_{\text{C,int}} \tag{3}$$

where

$$\delta\Pi_{\text{S,int}} = \int_{\Omega_0 \setminus \bar{\Gamma}_C} \mathbb{S} : \delta\mathbb{E}\, \mathrm{d}\Omega_0 \tag{4a}$$

$$\delta\Pi_{\text{C,int}} = \int_{\Gamma_C} \mathbf{T} \cdot \delta\boldsymbol{\delta}\, \mathrm{d}\Gamma_C \tag{4b}$$

and $\mathbf{T} = \boldsymbol{\sigma}\mathbf{n}$ denotes the Cauchy traction vector on the cohesive interface (i.e. the resolved Cauchy stress) in the current configuration, $\boldsymbol{\sigma}$ being the Cauchy stress tensor and $\mathbf{n}$ the normal to the crack flank. When the crack opening is small, there is no need to distinguish between two separating crack flanks. When the displacement jump is large, the geometric description of the process zone, with the possibility to detect contact between the blade and the material in the process zone, is required.

2.2. Crack propagation in solid-shell element mesh

8-node solid-shell elements are solid brick elements with a dimension, the thickness, significantly smaller than the other two. This allows to identify in an unambiguous way the two quadrilateral lower and upper surfaces. We assume that nodes 1-4, with coordinates gathered in vector $\mathbf{X}_{1-4}$, belong to the lower surface and nodes 5-8, of coordinates $\mathbf{X}_{5-8}$, to the upper one. To simplify the presentation, in an 8-node solid-shell element we define with the term "corner fiber" the segment connecting two nodes corresponding to each other on the element upper and lower surfaces. Each solid-shell element has then four corner fibers, whose midpoints define the corners of the element middle surface. Fiber midpoints

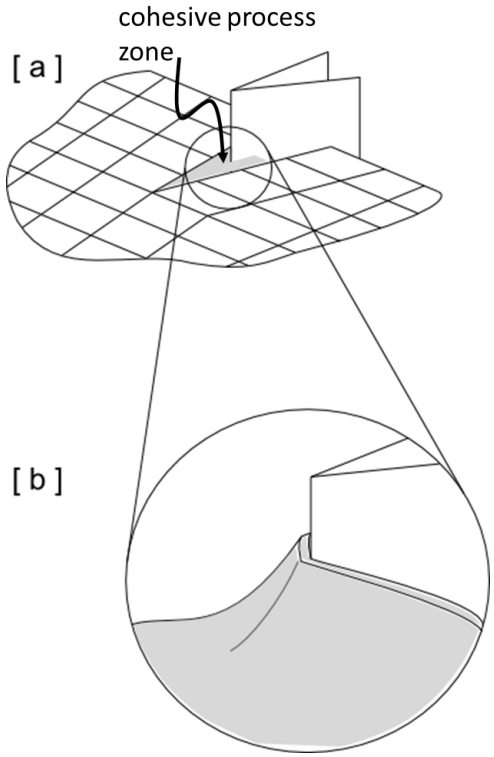

Figure 1: Two scales sketch of blade-process zone interaction. a) Finite opening of cohesive interface with cutting blade interfering with cohesive process zone. b) Mesoscale view of actual interaction.

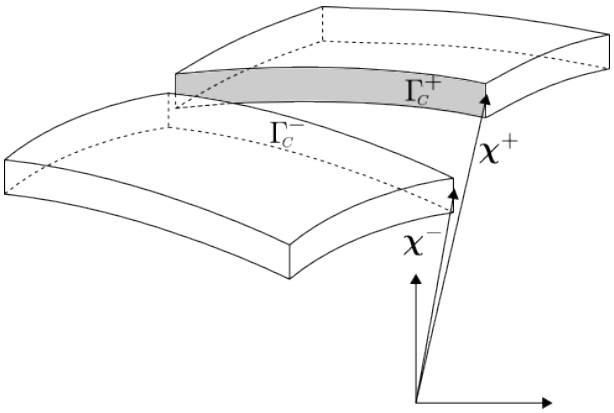

Figure 2: Opposite plus and minus crack flanks.

are termed "fiber nodes" and have coordinates $\mathbf{X}^m = (\mathbf{X}_{1-4} + \mathbf{X}_{5-8})/2$.

Two main assumptions are introduced: *i*) the shell thickness is so small that in the cohesive region its bending strength and through-the-thickness crack propagation can be neglected; *ii*) the specific surface work required for crack propagation due to cutting does not depend on the mode of fracture, so that only Mode I initiation and propagation can be considered in the cutting process (Atkins and Xu, 2005).

Based on these observations and assumptions, the proposed directional cohesive element approach can be described as follows. When a suitable fracture criterion is met at a given fiber node a, $a = 1, \ldots 4$,

the node belonging to that fiber is duplicated and it is assumed that cohesive forces $\mathbf{f}_a^{\pm}$ are transmitted between the newly created pair of fiber nodes $a^{\pm}$ by a massless string, i.e. a truss element ad hoc introduced in the model in correspondence of each pair of separating nodes (Figure 3). In view of the assumed small thickness, only one cohesive string through the element thickness, attached to the fiber nodes, is considered. Different options, in which strings are e.g. attached to Gauss points along fractured element faces, are however also feasible. In Frangi et al. (2010), cracks propagating in a mesh of classical 4-node shell elements were considered. In these elements, the nodes are placed in correspondence of the element middle surface, and the strings were directly attached to element nodes, without the need to define "corner nodes".

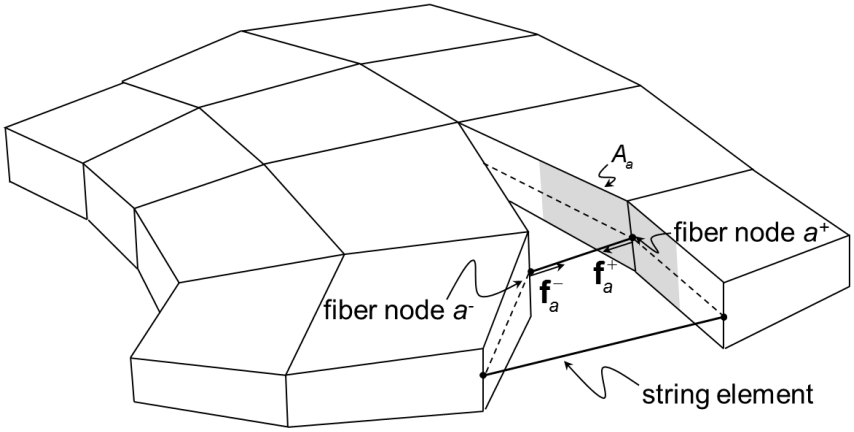

Figure 3: Directional cohesive elements connecting fiber nodes $a^{\pm}$ and pertinent cohesive surface A_a.

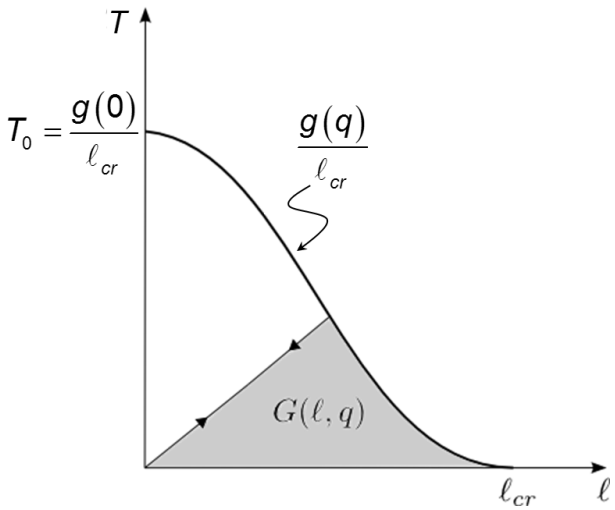

Figure 4: Cohesive law: softening function $g(q)$ and definition of available cohesive energy $G(\ell, q)$.

During the time steps which follow node duplication, the nodes separate and the string is a straight segment naturally endowed with a length ℓ which coincides with the distance between the nodes. The direction of the cohesive force is determined by the opening vector $\boldsymbol{\delta}$, while the intensity of the force

is $T(\ell)A_a$, where $T(\ell)$ depends on the specific cohesive constitutive law adopted for the string (such as, e.g., the one in Figure 4) and A_a is the area of the cohesive surface through the shell thickness pertinent to that node. It should be noted that in this case, since the traction and the opening displacement vectors are aligned, the lack of rotational equilibrium problem highlighted in Vossen et al. (2013) for large crack openings is not present.

The string element is a well defined geometric entity and its contact against the cutting blade can be checked throughout the analysis duration, even though, in view of the sharpness of the cutter and to enhance the procedure computational efficiency, contact is here only checked against the points belonging to the cutting edge (and not against the cutting sides). As in Frangi et al. (2010), when a point of a cable element is detected to be in contact with the blade, the string element is subdivided into two truss elements by introducing a joint in correspondence of the contact point (Figure 5). The length ℓ_a of the cable is now defined as the sum of the lengths ℓ_a^+ and ℓ_a^- of the two constituent truss elements. It is here assumed that the contact point cannot move along the cutting edge of the blade. Two forces $\mathbf{f}_a^+$ and $\mathbf{f}_a^-$ of the same magnitude are assumed to be transmitted by the two branches of the string to the crack flanks. The forces directions are however different at the two nodes a^+ and a^-, being determined by the directions $\mathbf{m}_a^\pm$ of the truss elements connecting the nodes to the contact point (see Figure 5b). The force magnitude in the cable is obtained from the stress in Figure 4 corresponding to the total cable length ℓ_a. In this way, the cohesive force can be transmitted between the crack flanks in a direction different from the line connecting the separating nodes, correctly taking into account the presence of the cutter. When the current length of the string exceeds the limit value ℓ_{cr} in Figure 4, the string is removed and no more cohesive forces are applied to the associated nodes.

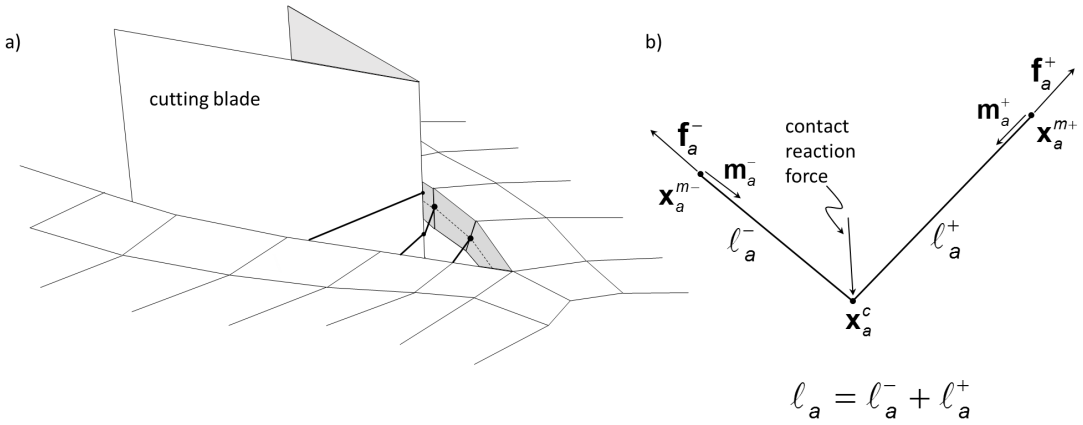

Figure 5: a) Cohesive string elements interacting with cutting blade. b) Force diagram after contact between cohesive string element and blade.

2.3. Cohesive force transmission

Let $\boldsymbol{\delta}_h = \mathbf{x}_h^+ - \mathbf{x}_h^-$ denote the distance between two separating nodes. Let $\theta \in [-1, 1]$ and $\zeta \in [-1, 1]$ be two intrinsic coordinates running on the crack surface Γ_C, with ζ running in the thickness direction. When the blade is not interacting with the cohesive process zone, the discretization of the cohesive internal work (4b) for the element e leads to

$$\delta\Pi^e_{\text{C,int}} = \int_{-1}^{1}\int_{-1}^{1} \mathbf{T} \cdot \delta\left[\sum_{h=1}^{4} N_h(\theta,\zeta)\boldsymbol{\delta}_h\right]^e J_{\Gamma_C}\, \mathrm{d}\theta\, \mathrm{d}\zeta \tag{5}$$

where J_{Γ_C} is the jacobian determinant for the area transformation on the crack surface and $N_h(\theta, \zeta)$, index h running on the four nodes of the element face coinciding with the crack flank, are the element interpolation functions restricted to the crack surface. The integral is performed using one integration point on the middle surface in the thickness direction and two integration points in the other direction (Newton-Cotes trapezoidal rule), i.e. at $(\theta = 1, \zeta = 0)$ and $(\theta = -1, \zeta = 0)$. According to this integration rule, the cohesive tractions are computed in correspondence of the fiber nodes belonging to opening crack faces. Unlike the classical shell elements used in Frangi et al. (2010), solid-shell elements can undergo thickness variations, dictated by the differential displacements of nodes belonging to the upper and lower surfaces. These variations are accounted for by the jacobian J_{Γ_C}, while, for the rest, in view of the conceptually identical used integration rule, the two formulations are equivalent.

Denoting $\square^m_a$ quantities evaluated at the fiber node $(\theta_a = 1, \zeta_a = 0)$ and $\square^m_b$ quantities evaluated at the fiber node $(\theta_b = -1, \zeta_b = 0)$, upon integration the contribution of element e to the cohesive internal work is expressed as

$$\delta\Pi^e_{\text{C,int}} = \left(\mathbf{f}_a \cdot \delta\boldsymbol{\delta}^m_a + \mathbf{f}_b \cdot \delta\boldsymbol{\delta}^m_b\right)^e \tag{6}$$

where $\mathbf{f}^e_a = (A_a \mathbf{T}^m_a)^e$ is the equivalent cohesive force at the fiber node $\mathbf{x}^m_a$ of element e, $A_a = w_a J^m_{\Gamma_C,a}$ is the crack surface area pertinent to the same fiber node, w_a is the integration weight and $\boldsymbol{\delta}^m_a = \sum_{h=1}^4 N_h(1,0)\boldsymbol{\delta}_h$ is the displacement jump at the same point. The fact that only one integration point has been used in the thickness direction accounts for the assumed small thickness and for the neglect of the bending cracking resistance. This low order integration rule is known to become inaccurate when the element size becomes large compared to the cohesive process zone, with the appearance of strong stress oscillations. Significantly better results could be achieved using a Newton-Cotes quadrature rule of higher order, such as the three-point rule (Do et al., 2013). In the present context, this would amount to introducing an additional string element at the centroid of the cohesive interface element. Even though this would not present conceptual difficulties, this possible improvement has been left for future implementations of the method.

The equivalent cohesive forces acting on the element nodes are obtained as usual through the virtual

work equivalence

$$\delta\Pi^e_{\mathrm{C,int}} = \sum_{h=1}^{4} (\delta\boldsymbol{\delta}_h \cdot \mathbf{f}_h)^e \tag{7}$$

with $\mathbf{f}^e_h = N_h(\theta_a, \zeta_a)\mathbf{f}^e_a + N_h(\theta_b, \zeta_b)\mathbf{f}^e_b$. The element nodal contribution has to be assembled with the other contributions coming from elements sharing the same pair of fiber nodes. Denoting by

$$\mathbf{f}_a = \mathop{\mathbf{A}}_e \mathbf{f}^e_a = \mathop{\mathbf{A}}_e (\mathbf{T}^m_a A_a)^e = \mathbf{T}^m_a \mathop{\mathbf{A}}_e A^e_a = \mathbf{T}^m_a A_a \tag{8}$$

the resulting force, as in Frangi et al. (2010) this is interpreted as being transmitted by a string element inserted at the middle surface between the separating fiber nodes, in the direction of $\boldsymbol{\delta}^m_a$ (see Figure 3).

At crack initiation, when the nodes are not separated yet, the string element is oriented in the direction of the average outgoing normal $\mathbf{n}_a$ to the crack flanks at $\mathbf{x}^m_a$ (Figure 6). The initial value $\mathbf{T}^m_{0a}$ of its force per unit area is set equal to the normal component of the Cauchy stress $\boldsymbol{\sigma}$ at the fiber node a, resolved onto the surface of normal $\mathbf{n}_a$.

$$\mathbf{T}^m_{0a} = \mathbf{n}_a \otimes \mathbf{n}_a \cdot (\boldsymbol{\sigma}(\mathbf{x}^m_a)\,\mathbf{n}_a) \tag{9}$$

In this way, only the traction normal component contributes to the cohesive resistance, but this is consistent with the assumption of prevailing Mode I conditions in the crack tip region and guarantees continuity of the normal stress component upon crack activation, avoiding spurious oscillations (Papoulia et al., 2003; Song and Belytschko, 2009). Immediately after crack activation and node duplication, the fiber nodes start to separate and the cohesive force, being transmitted to the flanks in the direction of the string element, is in general no longer normal to the flanks so that shear forces can be transmitted. The force transmitted by the string is equal on the two flanks only as long as the string does not interact with the blade. After blade contact, the force is transmitted to the flanks according to the "directional" concept (Figure 5b) and its direction is no longer equal on the two sides (it remains however equal in magnitude).

Denoting by $\mathbf{x}^c_a$ the position of the contact point between the blade and the string (Figure 5b), the current cohesive forces are given by

$$\mathbf{f}_a = \mathbf{f}^+_a = -\mathbf{f}^-_a = -\frac{\| \mathbf{f}_a \|}{\| \boldsymbol{\delta}^m_a \|}\boldsymbol{\delta}^m_a \qquad \text{no contact between blade and string} \tag{10a}$$

$$\left.\begin{aligned} \mathbf{f}^+_a &= f_a\,\mathbf{m}^+_a \\ \mathbf{f}^-_a &= f_a\,\mathbf{m}^-_a \end{aligned}\right\} \qquad \text{contact between blade and string} \tag{10b}$$

where

$$f_a = T^m_a(\ell_a)A_a, \quad \mathbf{m}^+_a = \frac{\mathbf{x}^c_a - \mathbf{x}^{m+}_a}{\| \mathbf{x}^c_a - \mathbf{x}^{m+}_a \|}, \quad \mathbf{m}^-_a = \frac{\mathbf{x}^c_a - \mathbf{x}^{m-}_a}{\| \mathbf{x}^c_a - \mathbf{x}^{m-}_a \|} \tag{11}$$

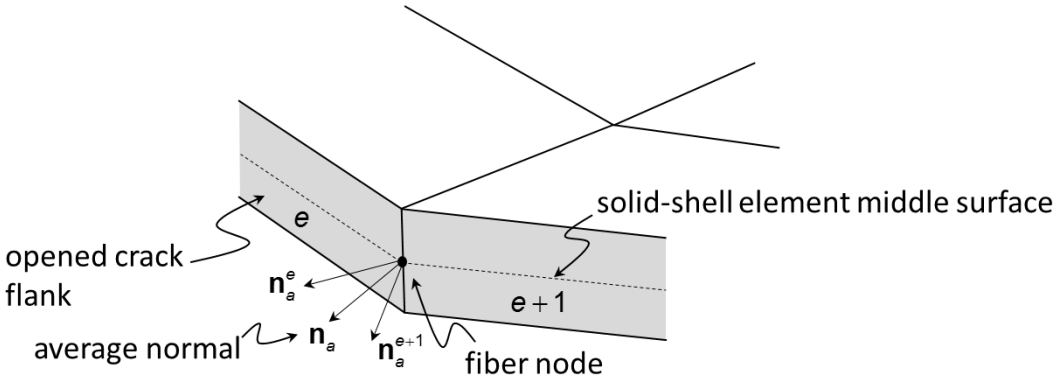

Figure 6: Average normal to the crack flank, evaluated at a fiber node, shared by elements e and $e+1$.

In the above definition of the cohesive forces, at each time step $\boldsymbol{\delta}_a^m$ and $\mathbf{x}_a^c$ are to be regarded as known quantities coming from the explicit integration of the equation of motion and the successive application of the contact algorithm, having in mind that the blade position in time is a priori assigned. The magnitude T_a^m is determined from the cohesive law, which will be discussed in the next section, on the basis of the known string total length

$$\ell_a = \| \mathbf{x}_a^c - \mathbf{x}_a^{m+} \| + \| \mathbf{x}_a^c - \mathbf{x}_a^{m-} \| = \ell_a^+ + \ell_a^- \tag{12}$$

Since the string elements are massless, equilibrium is statically preserved according to the force diagram in Figure 5b. Thanks to the adopted explicit time integration, the dynamic problem is solved at each time step at the macroscopic scale for assigned internal forces. The resulting displacements are then transmitted to the lower scale for the new determination of the internal cohesive forces.

3. Cohesive law

As discussed in the previous section, after crack opening the direction of the cohesive traction $\mathbf{T}_a^m$ applied at the fiber node $\mathbf{x}_a^m$ is defined by the orientation of the cohesive string segments at that node, which interact with the cutting blade, whereas its magnitude depends on the cohesive law which is described below. The magnitude T of the traction vector $\mathbf{T}$ can be expressed in general terms as a function of the crack opening through a cohesive potential $G(\ell, q)$, where ℓ is a scalar measure of the crack opening and q is an internal variable, such that $G_f = G(0,0)$ is the Mode I fracture energy. Following the formulation of the cohesive model proposed in Comi et al. (2006), a softening function $g(q)$ is introduced as

$$g(q) = -\frac{\partial G}{\partial q}(0,q), \quad \text{with } \frac{dg}{dq} \leq 0, \quad 0 \leq q \leq 1 \tag{13}$$

One defines $T_0 = g(0)/\ell_{cr}$ as the initial value of the normal traction at incipient crack propagation. Interpreting q as a progressive damage of the material in the cohesive process zone, g assumes the role of

the local rate of released cohesive energy. The resulting behavior is of the type shown in Figure 4, with complete recovery of the crack opening upon unloading.

For assigned q, $G(\ell, q)$ represents the cohesive energy remaining to be dissipated before complete fracture (see Figure 4). The damage q at time t is defined as equal to the ratio between the maximum attained crack opening and the ultimate opening ℓ_{cr}:

$$q(t) = \max_{\tau \le t} \frac{\ell(\tau)}{\ell_{cr}} \tag{14}$$

It should be noted that in the previous equation (14) the crack opening ℓ has to be intended in the sense defined in (12), i.e., as the total length of the cohesive string segment introduced between two separating nodes. This coincides with the displacement jump $\boldsymbol{\delta}$ only when the blade is not interacting with the string. Upon crack closure (unloading), the traction decreases linearly and vanishes for complete closure. The traction T is related to the crack opening ℓ by

$$T = \frac{\partial G(\ell, q)}{\partial \ell} \tag{15}$$

with the loading/unloading conditions

$$\left(T - \frac{g(q)}{\ell_{cr}}\right)\dot{q} = 0, \quad T - \frac{g(q)}{\ell_{cr}} \le 0, \quad \dot{q} \ge 0 \tag{16}$$

For $\ell/\ell_{cr} < q$ or $\ell/\ell_{cr} = q$ with $\dot{\ell} < 0$, the traction is then defined as

$$T = \frac{g(q)}{q}\frac{\ell}{\ell_{cr}}, \quad \dot{q} = 0 \tag{17}$$

For $\ell/\ell_{cr} = q$ and $\dot{\ell} > 0$ one has

$$T = \frac{g(q)}{\ell_{cr}}, \quad \frac{\dot{\ell}}{\ell_{cr}} = \dot{q} \ge 0 \tag{18}$$

In the simple case of a linear softening model (Figure 7), one can set

$$\begin{aligned}
G_f &= \frac{1}{2} T_0 \ell_{cr} \\
G(\ell, q) &= G_f + \frac{1}{2}\frac{T_0}{q}(1-q)\frac{\ell^2}{\ell_{cr}} - T_0 q\left(1 - \frac{1}{2}q\right)\ell_{cr} \\
g(q) &= -\frac{\partial G}{\partial q}(0, q) = T_0 (1-q)\,\ell_{cr} \\
T &= \frac{\partial G}{\partial \ell}(\ell, q) = \frac{T_0}{q}(1-q)\frac{\ell}{\ell_{cr}} = \frac{g(q)}{q}\frac{\ell}{\ell_{cr}^2} \quad \text{for } \frac{\ell}{\ell_{cr}} \le q,\ \dot{q} = 0 \\
T &= \frac{\partial G}{\partial \ell}(\ell, q) = \frac{g(q)}{\ell_{cr}} \quad \text{for } \frac{\ell}{\ell_{cr}} = q,\ \dot{q} \ge 0
\end{aligned} \tag{19}$$

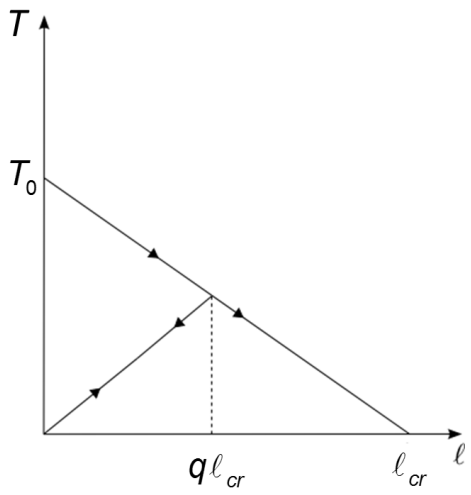

Figure 7: Example of linear softening cohesive model.

In the case of continuous loading, one has $\ell = q\ell_{cr}$ throughout the opening process and the expression of the cohesive potential becomes

$$G(q) = G_f - \frac{1}{2}T_0 q\ell_{cr} \tag{20}$$

where $\frac{1}{2}T_0 q\ell_{cr}$ is the fracture energy dissipated for a crack opening $\ell = q\ell_{cr}$ and $G(q)$ is the area of the shaded region in Figure 8.

Upon loading reversal, the crack can undergo partial closure, with $\ell < q\ell_{cr}$. In this case, the cohesive behavior is reversible (no dissipation) and the traction T is a linear function of ℓ. The second term in the potential $G(\ell, q)$ in $(19)_2$, which is quadratic in ℓ, defines the area of the shaded region in Figure 8b, while G_f and the third term play the role of inessential constants until ℓ reaches again the crack activation value $q\ell_{cr}$.

For the directional cohesive elements discussed in the previous section, the cohesive behavior is enforced at the fiber nodes $\mathbf{x}_a^m$. From the known configuration at the macroscale, one obtains the positions $\mathbf{x}_a^{m+}$ and $\mathbf{x}_a^{m-}$. From the solution of the contact problem within the process zone, one obtains $\mathbf{x}_a^c$ and then ℓ_a from equation (12). With these values and the previous history of the cohesive law at that point, which allows to define the current value of the internal variable q, one can compute T_a^m through (15) and then the equivalent internal nodal force through (10a) and (10b).

The initial traction T_{0a}^m depends on the current stress state in correspondence of crack activation at the considered fiber node $\mathbf{x}_a^m$. The current stress state is first extrapolated to the fiber node, then the assumed crack propagation criterion is checked. If the criterion is satisfied, the nodes on the element corner fiber are duplicated and T_{0a}^m is set equal to the normal component of the current Cauchy stress vector, according to equation (9). The fracture energy G_f, which can be dissipated in Mode I opening, is a material property and is attributed to the newly inserted string element, while ℓ_{cr} is defined according

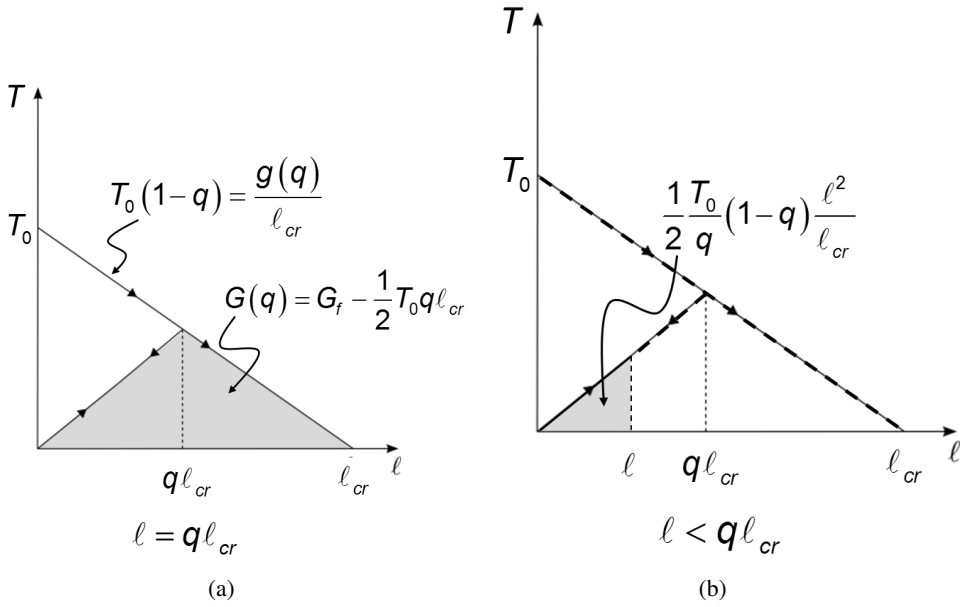

Figure 8: Cohesive model: a) crack opening with $\ell = q\ell_{cr}$; b) crack closing or re-opening with $\ell < q\ell_{cr}$.

to the assumed expression of $G(\ell, q)$ and to the values of G_f and T_{0a}^m. The new string element initially dissipates the same amount of energy that would be dissipated in the continuum model for a Mode I virtual opening of the two new crack sides. From this point onward, the continuum model is replaced by the discrete string element, which can elongate, get in contact with the cutting blade and dissipate energy.

4. Fracture initiation and propagation procedure

4.1. Fracture criteria

One of the main issues in the simulation of fracture processes is the definition and calibration of a fracture criterion. In the case of crack propagation in an elastic bulk material, the most used criterion is based on the evaluation of principal stresses. When a critical value is attained by the maximum principal stress at a point, a fracture begins to propagate orthogonal to its direction. This is the criterion that will be used in the second example of this paper, where crack propagation in a thin rubber sheet will be considered.

In ductile fracture, failure is the combined result of nucleation, growth and coalescence of microscopic defects. It is hence a progressive phenomenon, developing at the microscale, where, in the case of thin sheets, fracture is preceded by necking and which turns out to be strongly affected by such factors as the stress triaxiality, the Lode angle and the amount of accumulated plastic strains. Although material separation is in this case the result of complex physical processes occurring at the microscale, an accurate description of fracture propagation can be usually achieved using only variables at the macroscale, such as stress and strain components and their histories, giving rise to a number of different fracture

criteria. The literature on the subject is particularly abundant, also in view of its industrial impact, and its comprehensive review is outside the scope of this work. A recent review of the applicability of seven different fracture criteria can be found, e.g., in Wierzbicki et al. (2005).

Most ductile fracture criteria can be cast in the form

$$\int_0^{\varepsilon_f^p} F \, \mathrm{d}\varepsilon^p = C \tag{21}$$

where ε^p is the equivalent plastic strain, ε_f^p is its value at fracture, F is a function of the process parameters, such as e.g. stress triaxiality, and C is the critical value of the integral, which marks the onset of crack propagation. Simple specifications of the above general criterion are the plastic work criterion

$$\int_0^{\varepsilon_f^p} \sigma \, \mathrm{d}\varepsilon^p = C \tag{22}$$

and the widely used equivalent plastic strain criterion

$$\int_0^{\varepsilon_f^p} H(\sigma_H) \, \mathrm{d}\varepsilon^p = \varepsilon_{\mathrm{cr}}^p \tag{23}$$

which simply uses ε^p as the driving quantity for fracture initiation. The term $H(\sigma_H)$, H being the Heaviside function, has been here introduced to guarantee that fracture occurs only under tensile stress conditions. This latter criterion lacks of generality but it is easy to implement and it is often offered in commercial codes.

Localized necking is the main mechanism leading to fracture in ductile metal sheets. However, classical shell models cannot predict necking because out-of-plane stress components are neglected. This has been improved to a certain extent by the use of solid-shell elements, even though the elements are typically much larger than the localization width, so that not even in this case an accurate description of the threedimensional stress state in the necking region can be achieved. Despite its simplicity and these modeling difficulties, detailed validation tests carried out in Simonsen and Törnqvist (2004) have shown that the equivalent plastic strain criterion can give excellent results in the simulation of crack propagation in metal plates, provided that the equivalent plastic strain threshold is calibrated on suitable fracture tests. Furthermore, it has been pointed out that different values of the threshold should be used for crack initiation and for crack propagation. For these reasons, this criterion will be adopted in this paper for applications involving ductile materials, having in mind that more refined criteria, more suited for other types of materials, could be easily implemented in the proposed approach.

Since these criteria are based on a scalar measure of the accumulated damage, they do not provide any information on the direction of propagation. Therefore, crack propagation in the direction defined

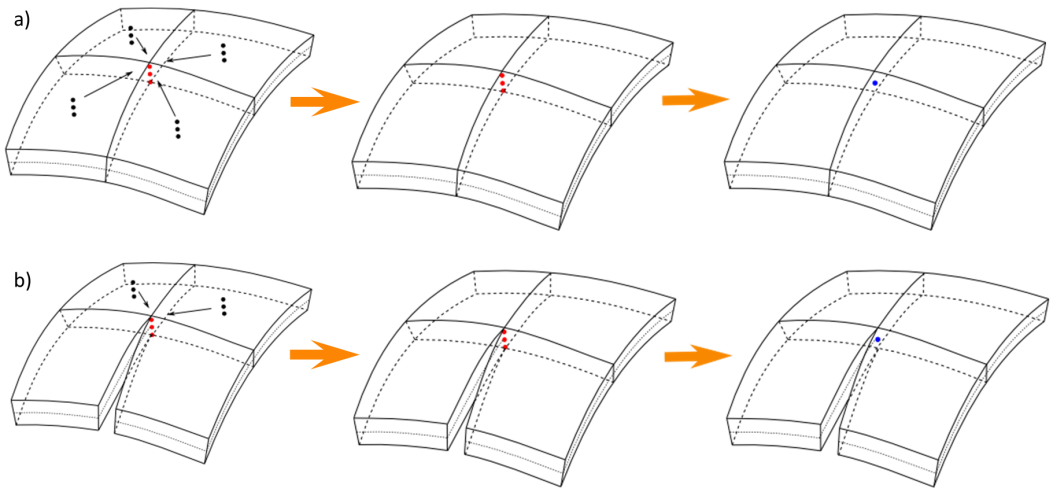

Figure 9: Extrapolation of nodal values: a) nodes belonging to uncracked elements, b) tip nodes.

by the direction of the maximum principal stress has been assumed in the applications.

4.2. Implementation of fracture criteria

The fracture initiation and propagation procedure is managed at nodal level. The verification of the propagation criterion, the determination of the fracture propagation direction and the definition of the initial value of the nodal cohesive force require to know the equivalent plastic strain and Cauchy stress at fiber nodes, having in mind that this information is stored at element Gauss points. The solid-shell element of Schwarze and Reese (2011) employed in this work makes use of one Gauss point in the in-plane dimension and of several Gauss points at different levels in the thickness direction. A possible strategy to compute fiber node values of stresses and strains starting from Gauss point values is illustrated below. Since experimental results show that nodes which are not at the tip of an existing crack may require a higher plastic deformation threshold than tip nodes (i.e. nodes at the uncracked tip of a cracked element side) to propagate a fracture (Simonsen and Törnqvist, 2004), different strategies are used in the two cases.

In the case of nodes shared by uncracked elements, an average nodal value of Cauchy stress and equivalent plastic strain is computed at each level in the thickness direction, considering all the elements sharing that node (see Figure 9a). The corresponding fiber node values are than obtained as the average of the values at the different levels along the corner fiber. The same procedure is used for the tip nodes, i.e. for nodes at the tip of an existing crack. The only difference is that in this case only values from the elements located ahead of the tip in the crack propagation direction are used (Figure 9b). Furthermore, a lower threshold value of ε_{cr}^{p} or of the critical principal stress, typically reduced by a 20% factor, is adopted for tip nodes.

When the fracture criterion is exceeded at a given fiber node A, the node is duplicated and the crack is assumed to propagate along the element edge whose normal is closer to the maximum principal stress

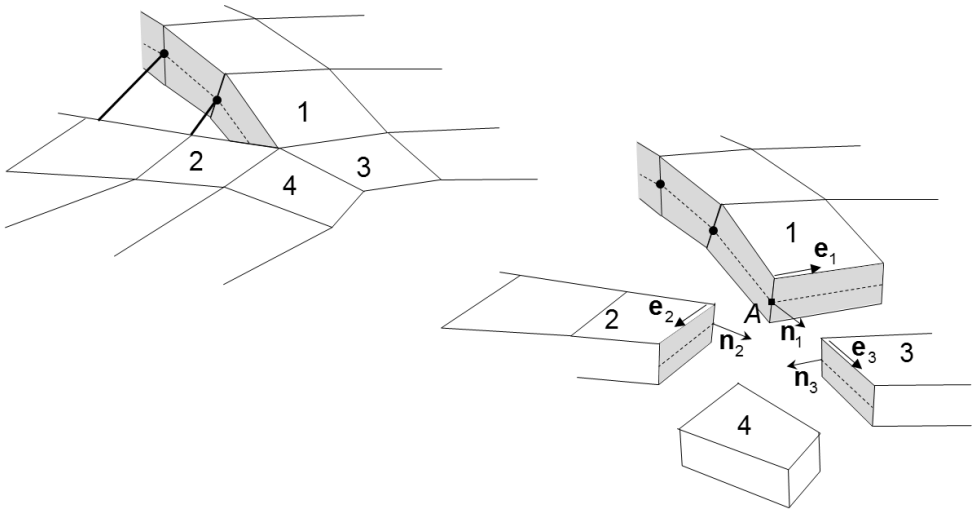

Figure 10: Definition of possible directions for crack propagation.

direction. Considering the crack tip in Figure 10, when the propagation criterion is satisfied, propagation can take place along anyone of the three element edges of directions $\mathbf{e}_1$, $\mathbf{e}_2$, $\mathbf{e}_3$ converging in the fiber node A, which represent the current crack tip. If $\mathbf{n}_1$, $\mathbf{n}_2$, $\mathbf{n}_3$ are the normals to the three element thickness faces of edges $\mathbf{e}_1$, $\mathbf{e}_2$, $\mathbf{e}_3$, in the applications propagation is assumed to take place along the edge whose normal is closer to the maximum principal stress direction, computed at the fiber node A using the averaging procedure described above (i.e., the direction of the maximum principal value of the average stress at A). When the fracture propagation criterion is exceeded at more than one fiber node in the same time step, only the node allowing fracture propagation in the direction whose normal is closest to the maximum principal stress direction is considered as a cracking node and is duplicated. In this case, the time step size is reduced to guarantee that forcing the opening of only one node in a time step does not affect the results. The time step size is then increased back to the original value in a fixed number of steps.

Once a node is duplicated, a cohesive string element is introduced at the middle surface between the new nodes with an initial strength defined according to equation (9).

5. Numerical examples

5.1. Crack propagation in a notched tube under internal detonation pressure

The first example of application of the proposed strategy deals with the dynamic fracture of a notched tube, a test which was considered for simulation also by Song and Belytschko (2009). Chao and Shepherd (2005) performed a series of experiments to study the fracture behavior of thin-walled and initially notched aluminum tubes to internal gaseous detonation loading. A number of experiments on aluminum 6061-T6 tubes, keeping constant the notch depth (0.56 mm), the notch width (0.3 mm), the tube size (0.88 mm thick, 38 mm in diameter and 914 mm long, as in Figure 11a) and loading conditions, but changing the notch length was conducted. Different fracture behavior was observed depending on the

notch length. In most cases, the forward (same direction as the detonation wave) and backward cracks propagated straight from the notch tip for some distance, then turned and ran helically around the tube. We have chosen to simulate shot 5 in Chao and Shepherd (2005), with initial notch $L = 12.7$ mm.

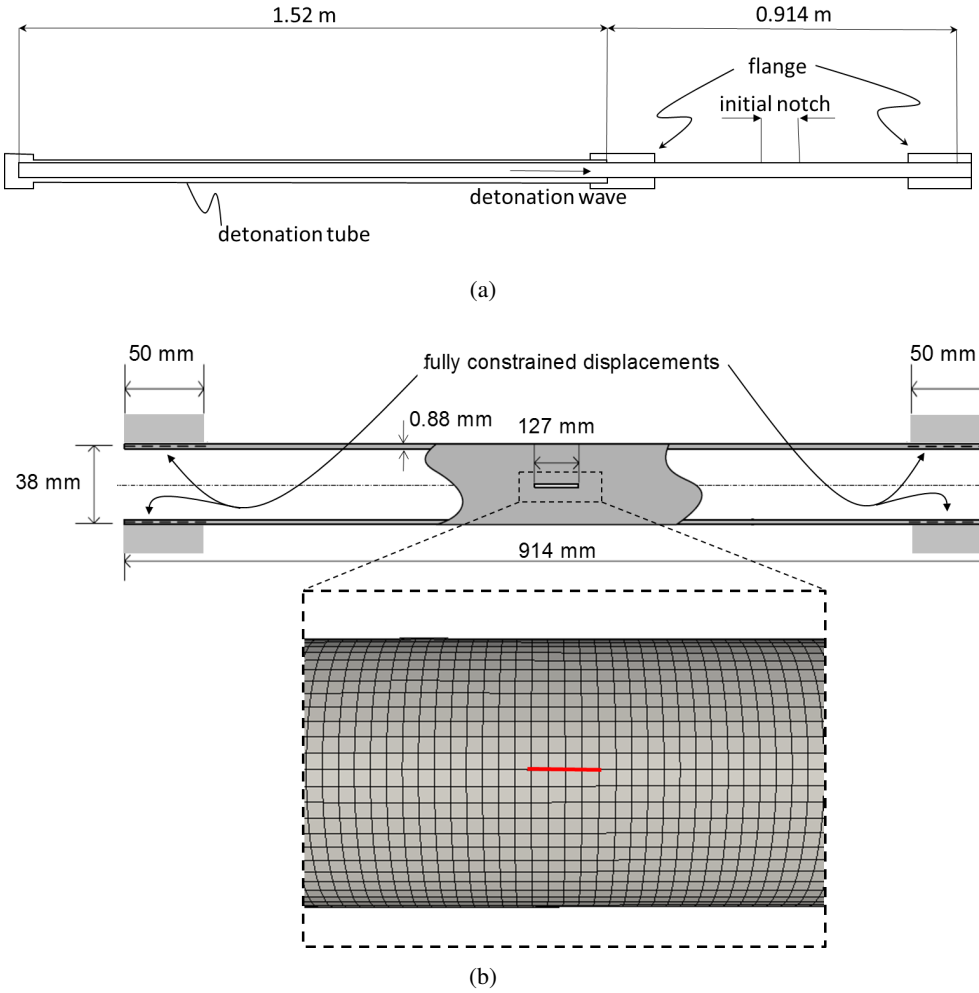

Figure 11: Notched tube fracture under internal detonation pressure. a) Tube assembly with 914 mm long specimen (Chao and Shepherd, 2005). b) Actual geometry considered for finite element model and detail of finite element mesh in notch region.

Even if our procedure has been developed for the simulation of cutting problems, it is important that the overall strategy is validated in situations where the crack path is not dictated by a blade. It is clear that in this case the introduction of "directional" cohesive elements is not necessary, and that other approaches could be more effective for this type of problems. In particular, the propagation direction is expected to be affected by the mesh layout.

The right part of the tube, which is included between two flanges (Figure 11b), has been discretized by a regular mesh of 26448 8-node solid-shell elements, of typical size of 2×2 mm, with only one element in the thickness direction. The presence of two flanges 50 mm long at the tube ends has been accounted for by suitable boundary conditions. The shell material has been modeled with J_2-plasticity,

density $\rho = 2.78 \cdot 10^{-9}$ Ns^2/mm^4, Young's modulus $E = 69000$ MPa, Poisson's ratio $\nu = 0.3$, yield stress $\sigma_y = 275$ MPa and by means of a linear isotropic hardening with constant slope $H = 640$ MPa. A cohesive fracture energy $G_f = 12$ kJ/m^2 has been considered on the basis of the critical stress intensity factor $K_{cr} = 30$ MPa $\sqrt{\text{m}}$, reported in Chao and Shepherd (2005). In order to avoid fragmentation, propagation starting from nodes not located at the tip of an existing crack has been penalized, as in Song and Belytschko (2009), by assigning a slightly higher toughness to those nodes. We considered a total ultimate strain $\varepsilon_u = 0.08$ taken from the literature for this type of aluminum. Considering a limit elastic strain $\varepsilon_y = 0.0039$, this gives an ultimate plastic strain $\varepsilon_u^p = \varepsilon_u - \varepsilon_y = 0.0761$. As in Song and Belytschko (2009), we used a critical total strain (i.e. the total strain at which a node is duplicated and the cohesive string is introduced) $\varepsilon_{\text{cr}} = 0.06\varepsilon_u$, which gives a cumulated critical equivalent plastic strain $\varepsilon_{\text{cr}}^p = \varepsilon_{\text{cr}} - \varepsilon_y = 0.0036 = 0.047\varepsilon_u^p$ to be used for the crack propagation criterion (23). Moreover, we modeled the notch as machined through the entire depth of the shell even if in the experiment it had a depth of 0.56 mm in a total thickness of 0.88 mm.

Beltman and Shepherd (2002) provided a pressure time history function $p(x,t)$ suitable to model the detonation wave:

$$p(x,t) = \begin{cases} 0, & t < x/v_{cj} \\ p_{cj} \exp(-(t - x/v_{cj})/T_0), & t > x/v_{cj} \end{cases} \tag{24}$$

where x is the axial distance from the detonation source to the material point, t the simulation time, $T_0 \approx 3x/v_{cj}$ is the pressure decay time and p_{cj} and v_{cj} the Chapmand-Jouguet pressure and detonation wave propagation velocity, respectively. For the simulation we used $p_{cj} = 6.2$ MPa and $v_{cj} = 2390$ m/s to model internal detonation wave, as in Song and Belytschko (2009).

Figure 12 shows a comparison of the final deformed shape between the simulation and the experimental results. The two pictures have been reproduced at the same geometric scale in order to provide a clear visual comparison. Despite some expected discrepancies in the crack path, the simulation is in relatively good qualitative agreement with the experiment, also in terms of crack propagation path length. The numerically computed lengths of the crack paths traveled from the notch tips are: 234 mm forward and 142 mm backward. These lengths have been computed by counting the number of cracked element sides in the final configuration, assuming a length of 2 mm for each side, and have to be compared to the corresponding values measured in the experiments: 224 mm forward and 168 mm backward, as reported in Table 6 of Chao and Shepherd (2005). This small difference and the fact that, as in the experiment, the cracks arrested before severing the tube in different parts, seem to confirm that an approximately correct amount of energy is dissipated by the numerical model.

5.2. Cutting of a rubber sheet by a wedge

Lake and Yeoh (1978) conducted a series of experiments for assessing the resistance of pre-stretched

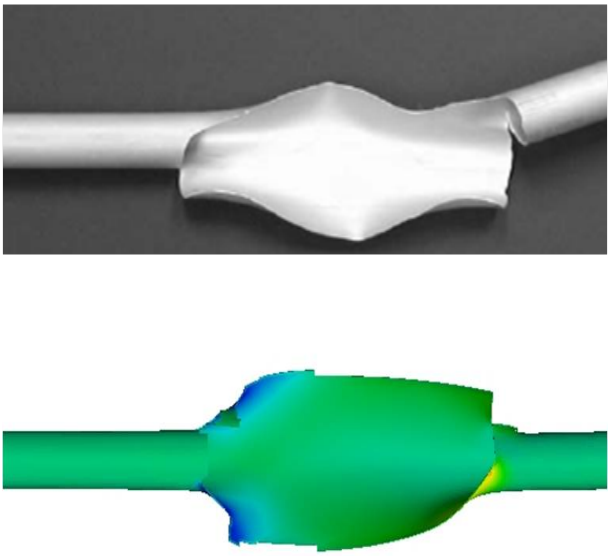

Figure 12: Notched tube fracture under internal detonation pressure. Comparison of final deformed shapes. Above: shot 5 in experimental campaign (Chao and Shepherd, 2005). Below: simulation result.

rubber sheets (Figure 13) to blade cutting, under conditions where friction is minimized. The propensity to buckling of thin rubber sheets required the adoption of razor blades as cutting implements, together with a pre-stretching of the rubber sheets to ensure the specimen cutting. In particular, the existence of a minimum value of pre-stretching elastic strain energy, below which no crack propagation could be obtained, was pointed out. On the other hand, a threshold value of elastic strain energy above which unstable crack propagation takes place, was also estimated. These features become evident if the rubber sheet is cut by a razor. Unfortunately, the low order solid-shell elements used in this work are not sensitive to the blade sharpness since they cannot resolve the local stress intensification due to blade contact, unless the blade edge radius of curvature is of the order of the element size. Moreover, the experimental results reported by Lake and Yeoh (1978) were obtained applying a constant force to the blade, leading to unstable cutting of natural rubber specimens, whose mechanical properties were not completely specified in the paper. For these reasons, it has not been possible to precisely simulate the experimental tests. Using material properties taken from the literature and a wedge shaped blade, with a curvature radius of 0.1 mm (Figure 14), we have rather tried to reproduce in the simulation the existence of a transition from combinations of pre-stretching and rubber strength leading to a clean cut, to those leading to severe buckling, with the impossibility to cut the sheet.

In our investigation we have adopted a pre-stretched rubber sheet 32 mm wide, 40 mm long, 0.1 mm thick, with a pre-formed crack of 5 mm parallel to its long edges (Figure 13). We have considered a low quality rubber with properties taken from the literature, whose constitutive behavior is described by a compressible Neo-Hokean model (see e.g. Holzapfel, 2000, chapt. 6.5), with strain energy function Ψ

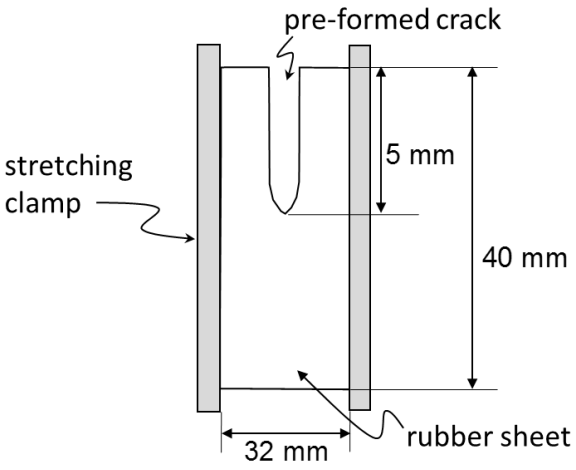

Figure 13: Cutting of a rubber sheet. Test pieces used for cutting measurements, Lake and Yeoh (1978), and geometric dimensions of adopted numerical model (not at right scale).

defined as

$$\Psi(I_1, J) = \frac{\mu(1-2\nu)}{2\nu}\left(J^{-\frac{2\nu}{1-2\nu}} - 1\right) + \frac{\mu}{2}(I_1 - 3) \tag{25}$$

where I_1 is the first invariant of the left Cauchy-Green tensor, J is the determinant of the deformation gradient, $\mu = 1$ MPa is the shear modulus and $\nu = 0.49$ is Poisson's coefficient. A material density $\rho = 1 \cdot 10^{-9}$ Ns^2/mm^4 has been assumed. A reference tear strength of $T_0 = 2.0$ N/mm^2 has been used associated to a fracture energy $G_f = 3$ N/mm. A crack initiation/propagation criterion based on the maximum principal stress has been adopted.

The sheet has been discretized by means of 6514 solid-shell elements, mainly concentrated along the expected fracture path around the symmetry axis (Figure 14). The wedge has been assigned a constant velocity of 96 mm/s which is much faster than the real blade velocity reported in the experiments (of the order of mm/hr). We have conducted two distinct simulations keeping constant the fracture energy and the initial pre-stretching of 5.76 mm (corresponding to a uniform nominal strain of 18%) and varying

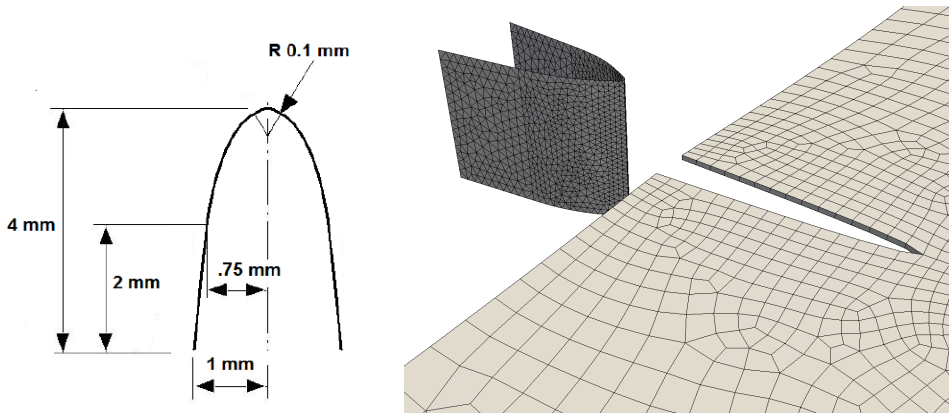

Figure 14: Cutting of a rubber sheet. Blade geometry.

the tear strength of about 20%. As expected, we have obtained a completely different behavior of the specimen in the two cases. In the first case (Figure 15), with a tear strength $T_0 = 2.0$ N/mm^2 a stable cutting has been obtained. After the initial pre-stretching, only the first two nodes at the tip of the pre-formed crack reached the critical condition and have been duplicated. A stable crack started to develop as soon as the blade got in contact with the plate. The contact of the blade also produced a local buckling of the material in front of the tip, with the wavy plate deformation clearly visible in Figures 15b and 15c. The interaction between the blade and the cohesive strings can be appreciated in Figure 16, which refers to the end of the analysis, corresponding to a propagation of about 20 mm.

Considering a 20% higher tear strength $T_0 = 2.4$ N/mm^2, a completely different response has been obtained. The initial plate configuration after the pre-stretching phase was almost the same as in the previous case, but in this case there were no cracked nodes. After contact, the blade did not succeed in promoting crack propagation. The blade contact produced a compression state ahead of the tip with the extensive buckling visible in Figure 17. Further blade advancement drew the material which folded with severe wrinkles as in Figure 18. At this point the analysis stopped, because no self-contact capabilities for the elements upper and lower surfaces were implemented in the code.

Even though a quantitative comparison with the experimental results has not been possible, the simulation has confirmed the existence of different cutting regimes depending on the relative magnitude of the tear resistance and the initial pre-stretching.

5.3. Cutting of a metal plate by a wedge

The cutting of a thin metal plate by a wedge, such as the one carried out in experiments described in Lu and Calladine (1990), has been simulated. The basic geometrical features of the cutting set-up are shown in Figure 19, where $\alpha = 10°$ denotes the blade tilting angle with respect to the plate, $2\theta = 10°$ the wedge opening angle and $2B = 10$ mm the width of the wedge shoulder. The tilting angle α is used to favor a clean cut of the plate. We have considered a mild-steel specimen, with a thickness of 0.5 mm, occupying an area of 215×200 mm. As in the experiments, the plate has been pre-cut for a length of 25 mm and the two sides of the cut have been slightly bent upward in the initial configuration (Figure 20) to facilitate the initiation of the cutting process. Young's modulus $E = 210000$ MPa, Poisson coefficient $\nu = 0.3$, material density $\rho = 7.5 \cdot 10^{-9}$ Ns^2/mm^4 have been assumed, together with a perfectly elasto-plastic Mises model with a yield stress of 272 MPa, a critical equivalent plastic strain $\varepsilon^p_{cr} = 0.15$ and a cohesive fracture energy $G_f = 353$ N/mm with linear softening. The plate has been discretized with 4156 8-node solid-shell elements, mainly concentrated along the expected fracture path, where the element in-plane size is of about 1.5×1.5 mm.

Contact conditions between the rigid cutting tool and the deformable shell are enforced by means of a penalty approach with a penalty coefficient equal to $\lambda = 2 \times 10^5$ N/mm^3.

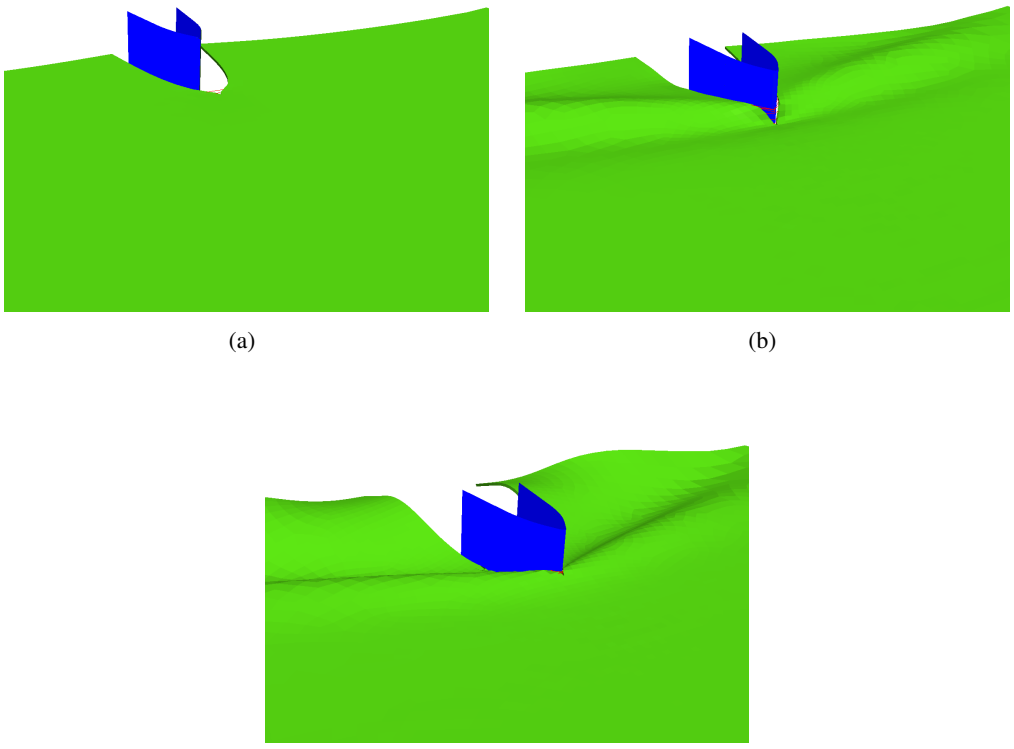

(a) (b)

(c)

Figure 15: Cutting of a rubber sheet. Evolution of the stable cutting process for tear strength $T_0 = 2.0$ N/mm^2.

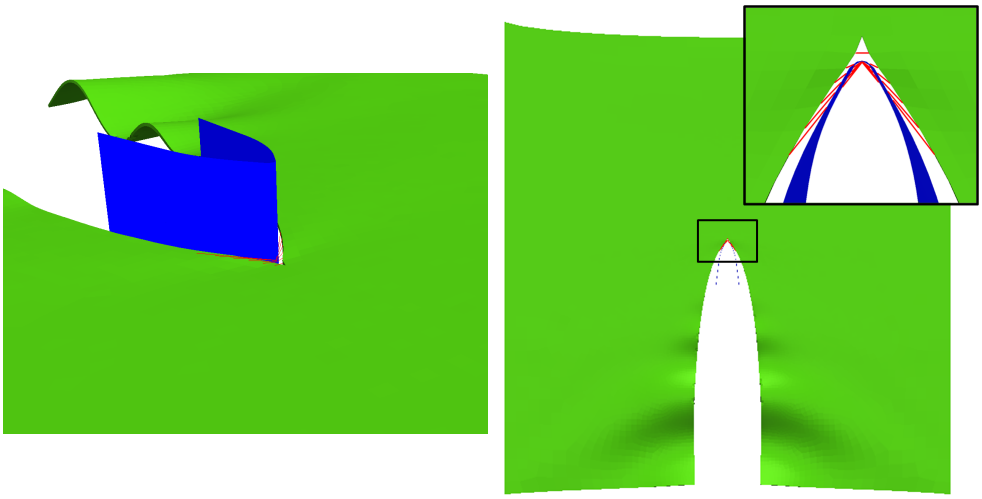

Figure 16: Cutting of a rubber sheet. Final snapshots of the stable cutting process for tear strength $T_0 = 2.0$ N/mm^2.

The plates cut in the experiments were relatively thick, with thicknesses up to 2.0 mm, too thick for our approach, with only one cohesive string element through the thickness. Therefore, the cutting of a 0.5 mm thick plate, which was not considered in the experiments, has been simulated. A quantitative validation of the numerical model has been obtained using the analytical formula in the absence of friction

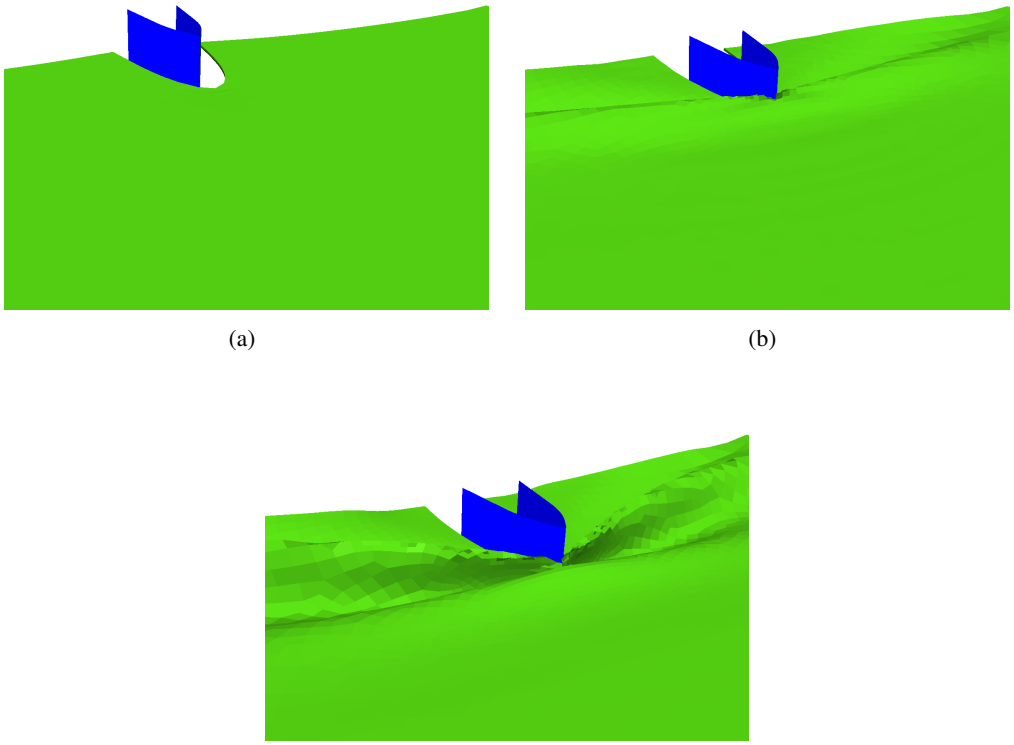

(a) (b)

(c)

Figure 17: Cutting of a rubber sheet. Evolution of buckled configuration for tear strength $T_0 = 2.4$ N/mm^2.

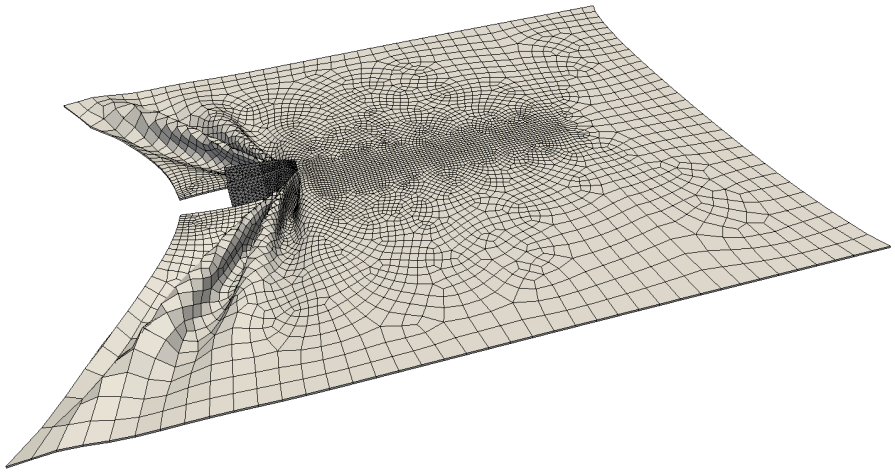

Figure 18: Cutting of a rubber sheet. Buckled configuration for tear strength $T_0 = 2.4$ N/mm^2.

presented in Simonsen and Wierzbicki (1998) to compute the resisting force F to wedge penetration:

$$F = \frac{0.64}{\sqrt{3}}\sigma_y tR\cos^2(\theta)(1 + 0.55\theta^2) + \frac{2}{\sqrt{3}}\sigma_y tB\theta + \frac{\sigma_y t^2(B+R)}{\sqrt{3}R\cos\theta} \tag{26}$$

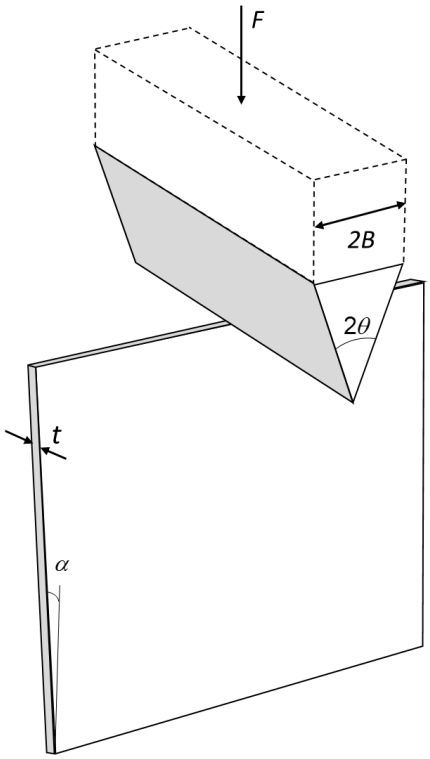

Figure 19: Cutting of a metal plate by a wedge. Schematic view of plate specimen about to be cut by a wedge (Lu and Calladine, 1990). Dashed lines define wedge shoulders not considered in finite element model.

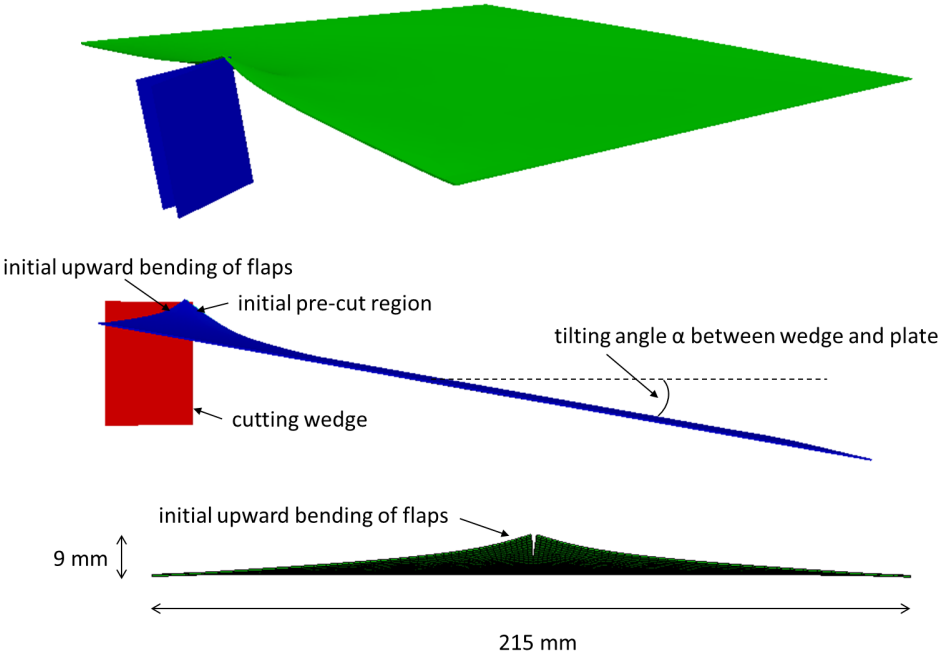

Figure 20: Cutting of a metal plate by a wedge. Schematic views of plate specimen with inclination of $\alpha = 10°$ with respect to wedge. Last rear view shows initial 9 mm upward bending of flaps along edges of pre-cut region.

where t is the plate thickness and R is the rolling radius of the lateral flaps, defined as

$$R = \sqrt{\frac{Bt}{0.64(1 + 0.55\theta^2)\cos^3\theta}} \tag{27}$$

Equation (26) has been derived assuming a rigid-plastic behavior, in the absence of friction, and imposing that the external loads power equals the rate of energy dissipated by plastic deformation and fracture. The first term in equation (26) is due to the cohesive energy dissipation in the tip zone while the other two terms come from the energy dissipation due to membrane and bending plastic deformation, respectively. The latter contribution is due to the plastic rolling of the lateral flaps.

Substituting in (26) the parameters of our example, a force equal to $F = 373$ N is obtained. In the simulation, the resisting force on the wedge has been computed as the resultant of the contact forces on the wedge. Due to the discretization, these exhibit strong oscillations which we have partially smoothed in Figure 21, where numerical results have been compared to the theoretical value from (26), by a mobile averaging with basis equal to the element length. It can be observed that the numerical force oscillates around the theoretical value, providing a quantitative validation of the numerical procedure.

The oscillations in the evolution of the numerical force are a consequence of the discrete contact between plate and blade, with the consequent sudden application of high penalty forces, and of the discrete release of energy occurring when nodes are duplicated and the cohesive elements are introduced in the discretization. This effect is emphasized by the relatively large element size of about 1.5×1.5 mm when compared to the blade sharpness. In Frangi et al. (2010), it was shown as the use of finer mesh can allow to reduce stress oscillations. It should be noted however, that the possibility of using relatively large elements is one of the motivations at the basis of the proposed approach. As mentioned in Section 2.3, stress oscillations due to continuum-discontinuum transition could probably be mitigated by considering an additional cohesive string at the centroid of the separating element side (Do et al., 2013). An alternative provision, based on the introduction of correction forces to the balance equation, to smoothly release the tip element while the crack tip is traveling through the element, has been proposed by Menouillard and Belytschko (2010) and applied to crack propagation in shells by Mostofizadeh et al. (2013). Improvements in this sense are currently under study and will be considered in a future work.

The contour plots of the equivalent plastic strain in Figure 22, show the qualitatively correct plastic folding of the lateral flaps, which is in agreement with the dissipation mechanism assumed in equation (26). The lateral view in Figure 22 shows the rise of the lateral flaps as a consequence of the passage of the wedge shoulders and of the wedge inclination with respect to the plate plane. Figure 23 provides a qualitative comparison between the final cutting patterns obtained in an experiment carried out in Lu and Calladine (1990), on a metal plate 1.6 mm thick, and in the numerical simulation. Good qualitative agreement is observed.

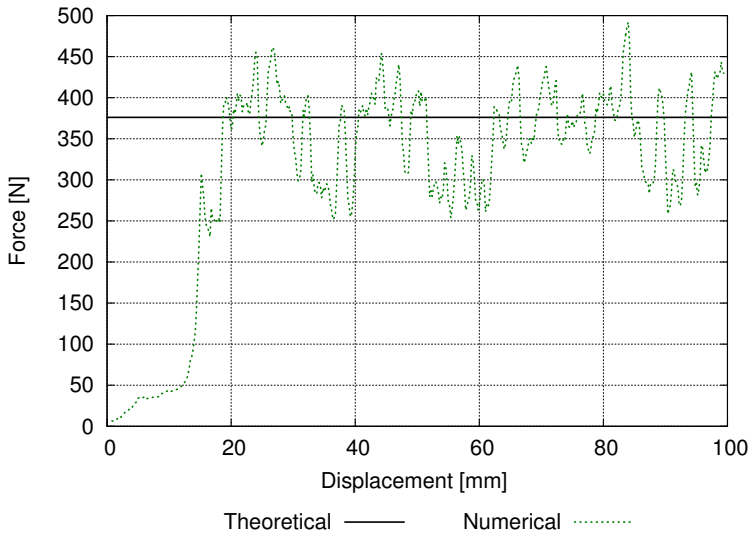

Figure 21: Cutting of a metal plate by a wedge. Reaction force on the rigid wedge vs. wedge penetration. Horizontal solid line obtained from (26).

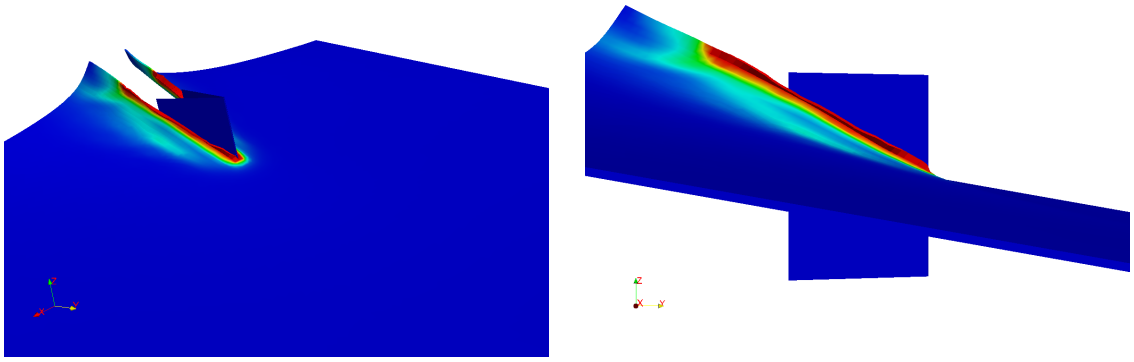

Figure 22: Cutting of a metal plate by a wedge. Contours of equivalent plastic strain.

5.4. Cap opening of a carton package

We focus on the simulation of the cap opening process of a carton package of the type shown in Figure 24a. This problem has been already considered in Frangi et al. (2010), where classical elastic shell elements were used rather than elastoplastic solid-shell elements as in the present work. Thanks to a screw thread, when the cap in Figure 24b is rotated, the blades shown in Figure 24c, made of HDPE (High Density Poly-Ethylene), undergo a downward rotating motion, cutting a thin membrane in a region of the package where a hole has been pre-laminated in the paperboard (Figure 24a). The membrane used to seal the package is in this case a layered composite, with a total thickness ranging from 70 to 78 μm, made of a thin aluminum layer (6-9 μm) and various low-density polyethylene (LDPE) coating layers. A typical response of a uniaxial test on one of these materials is shown in Figure 25. The two curves, obtained by specimens extracted in lamination (machine) direction (MD) and cross-machine (CD) direction, are close to each other, showing that the laminate material is only mildly anisotropic. After a nominal stress

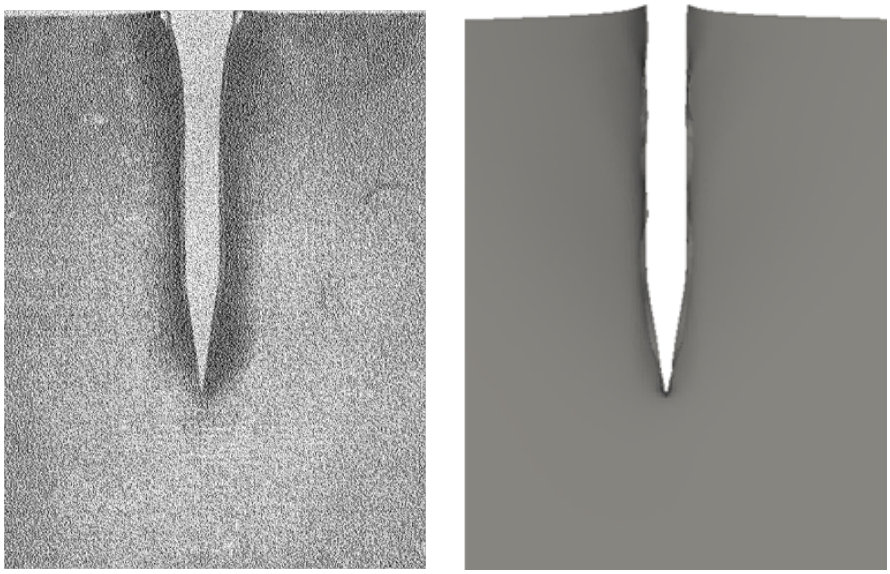

Figure 23: Cutting of a plate by a wedge. Qualitative comparison of fracture pattern in experiment (left, taken from Lu and Calladine, 1990, Figure 4) and numerical simulation (right).

peak is reached, a sudden drop is observed, corresponding to the rupture of the aluminum layer, followed by a long plateau, usually corresponding to the occurrence of localized necking deformation, where the molecules of the LDPE realign along the direction of loading. The limit nominal strain of 500% corresponds to the cross-head limit of the testing rig and not to the failure of the specimen, which has a typical failure nominal strain of 700-900%.

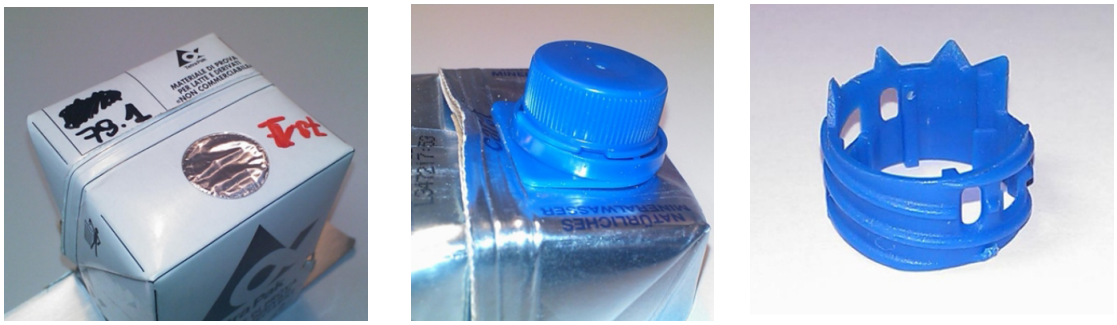

(a) (b) (c)

Figure 24: Cap opening. Opening system: a) package with pre-laminated hole (PLH); b) applied cap; c) cutting HDPE teeth.

We have analyzed a circular membrane, composed of aluminum and LDPE layers, of radius $R = 10.2$ mm and thickness $h = 0.074$ mm, which is assumed to be clamped on the outer boundary. The real membrane has an initial slackness due to the manufacturing process. To reduce the initial stiffness in the finite element model, accounting in this way for the slackness of the real membrane, the modeled membrane has a diameter which is about 14% larger than the real one. The cutting tool is depicted in Figure 24c and has an average radius of 9.4 mm. The radius of curvature at a blade edge is approximately of 0.1 mm. The tool is treated as a rigid body undergoing a prescribed rotation and vertical displacement

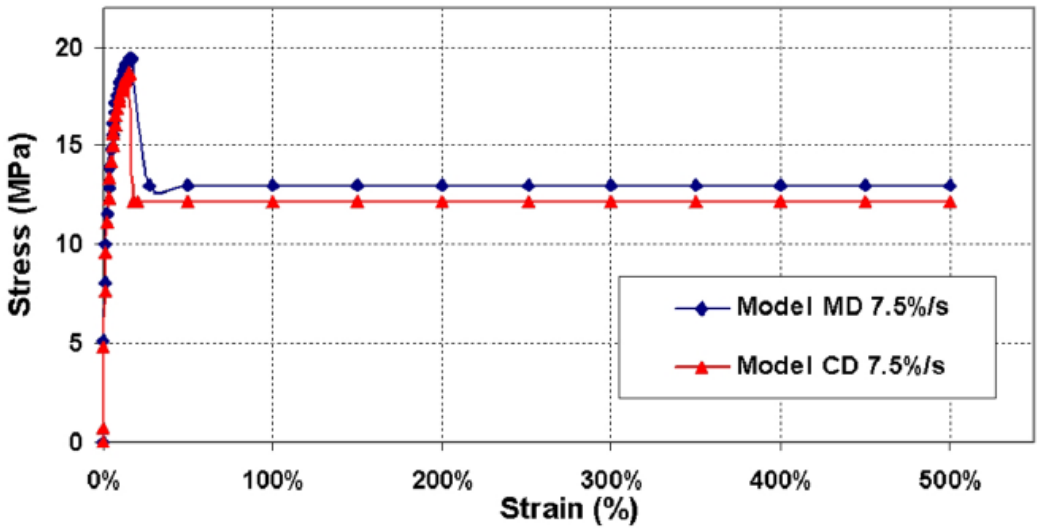

Figure 25: Cap opening. Typical uniaxial response of layered composite for food packaging.

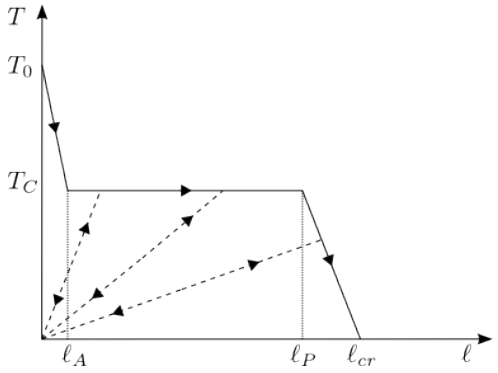

Figure 26: Cap opening. Constitutive modeling of cohesive element for cutting simulation.

simulating the true opening process. The membrane has been discretized with 2634 solid-shell elements. The results of the simulation have been validated against the outcome of an experimental campaign, whereby the torque applied to the opening cap has been measured versus the produced rotation.

The composite lamina is simulated as an equivalent homogenized and isotropic membrane with Young modulus $E = 1768$ MPa, Poisson coefficient $\nu = 0.3$ and a density of $\rho = 2 \times 10^{-9}$ Ns^2/mm^4. The hardening behavior is modeled by means of the following evolution of the yield limit $\sigma_y(\varepsilon^p)$

$$\sigma_y(\varepsilon^p) = \sigma_{y0} + Q\,(1 - \exp(-\varsigma\varepsilon^p)) \tag{28}$$

in which $\sigma_{y0} = 11$ MPa is the initial yield stress, $Q = 40$ MPa the saturation parameter and $\varsigma = 6.63$ the hardening exponent.

The adopted cohesive behavior in string elements, reproducing the experimental observation in Figure 25, is shown in Figure 26, with $T_0 = 18$ MPa, $T_C = 12$ MPa, $\ell_A = 0.5$ mm, $\ell_P = 3$ mm and

ℓ_{cr} = 4 mm. These have been obtained assuming a fracture energy G_f = 30 N/mm for the aluminum layer and G_f = 45 N/mm for the LDPE layers, leading to a homogeneized fracture energy G_f = 43.5 N/mm, which corresponds to the area beneath the curve in Figure 26: $(1/2)(T_0-T_C)\ell_A+(1/2)T_C(\ell_P+\ell_{cr})$. These are the same parameters adopted in Frangi et al. (2010), where the issue of parameters choice has been briefly discussed.

The comparison between the numerical predictions and experiments in terms of applied torque vs. rotation angle is presented in Figure 27. Good agreement is achieved everywhere, with the exception of the initial part of the diagram, between the experimental result (black solid curve) and the result obtained using directional cohesive elements (dotted curve). Indeed, no friction between the rotating teeth and the membrane is incorporated in the model and this explains the initial difference between the two curves: at the beginning of the cap rotation, the teeth are not in contact with the membrane and the initial torque value is entirely due to friction in the screwing system. Also in this case the numerical curve exhibits some oscillations, which however are less pronounced than those of the experimental curve. As it was shown in Frangi et al. (2010), numerical stress oscillations can be reduced to a certain extent by considering a finer mesh.

The importance of the role of the directional cohesive elements can be fully appreciated from the third curve in Figure 27 (red curve), where the results obtained using classical cohesive interface elements are shown. In this case, the cohesive force is transmitted along the direction of the line connecting the separating pair of nodes, and no interaction between the cutting blade and the cohesive process zone is accounted for. This is clearly visible in Figure 28, where snapshots at synchronized instants of the analysis with (a) and without (b) directional cohesive elements are shown. In the latter case, the line of action of the cohesive forces passes through the blades, without any interaction. In view of the high ductility of polyethylene, in most of the cohesive interfaces the crack opening produced by blade contact against the separating crack flanks is not enough to reach the ultimate opening ℓ_{crit} = 4 mm. The consequence is that the crack remains partially closed along most of the crack path and only a limited amount of the available fracture energy is dissipated, as it is evident from the plot in Figure 27. Unlike in the previous case, when directional cohesive elements are used the blade interacts with the process zone and cohesive forces are transmitted in a modified direction, dissipating the correct amount of energy (Figure 28a). This result shows that the use of standard cohesive interfaces may be not adequate for the simulation of this type of problems. A visual comparison between photos of one of the experiments, taken from the inside of the package during the opening process, and snapshots of the simulation with directional cohesive elements is displayed in Figure 29 which, again, shows a good qualitative agreement in terms of fracture pattern and advancement. Photos from experiments and numerical snapshots are synchronized with the physical time.

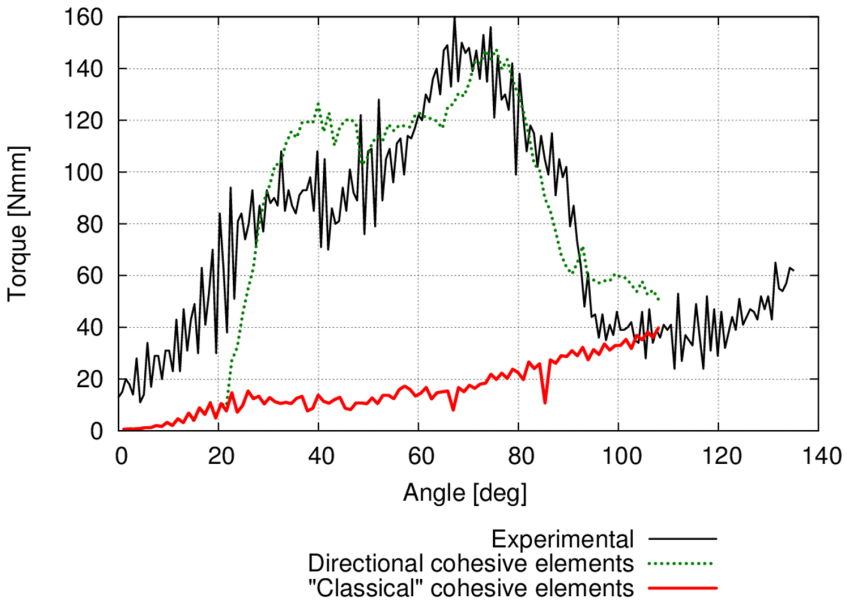

Figure 27: Cap opening. Torque vs rotation angle graph. Experiments (black solid curve) vs. numerical results obtained using: directional cohesive elements (dotted curve); "classical" cohesive elements (red, or gray in black and white printing, solid curve).

6. Conclusions

This work has been devoted to the development of a numerical tool in an explicit dynamics framework to efficiently simulate the blade cutting of thin-walled elastoplastic structures. In view of possible future consideration of delamination processes, the concept of "directional" cohesive elements, previously introduced in Frangi et al. (2010) for the cutting of elastic shells, has been revisited and re-implemented for application in conjunction with elastoplastic solid-shell elements. The solid-shell element Q1STs (Schwarze and Reese, 2011), partially reformulated for the implementation in an explicit framework (Pagani et al., 2013), has been used for the discretization of the bulk material.

Directional cohesive elements have been shown to represent an effective simplified approach at the macroscale which, with relatively coarse meshes, allows for the resolution of the complex interaction occurring between the cutting blade and the cracking material in the cohesive process zone at the scale of the shell thickness. Whenever a crack is opening, cohesive string elements are introduced between the separating nodes. These elements are geometric entities which can be monitored throughout the analysis to detect possible contact with the blade. When this happens, the string elements transmit forces in a straightforward way to the crack flanks in different directions. The intensity of the transmitted forces is determined by a cohesive constitutive behavior which has to be calibrated on the basis of the material fracture energy. Since tractions transmitted by the cohesive string elements and opening displacement vectors are aligned, problems of lack of rotational equilibrium are avoided in the case of large crack openings. An operative strategy for the treatment in the numerical model of quasi-brittle and ductile

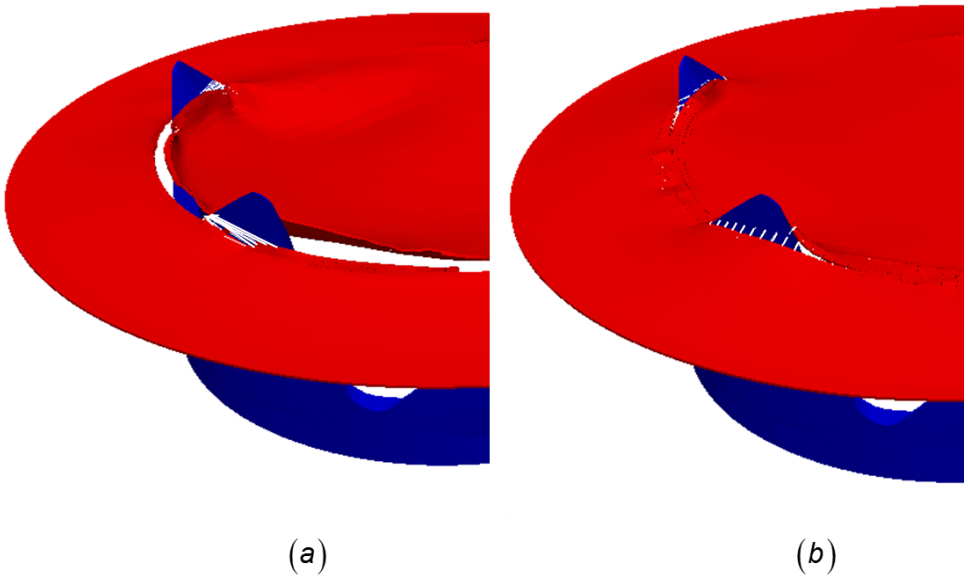

Figure 28: Cap opening. Snapshots at synchronized instants, obtained with: a) directional cohesive elements; b) classical cohesive interface elements. White segments represent direction of cohesive forces.

crack initiation and propagation has been developed and illustrated.

The proposed approach has been validated against several experimental tests of engineering interest, showing encouraging accuracy and versatility and confirming the general validity of the proposed methodologies.

Further studies on the simulation tool are currently in progress to remove some of the limitations of the present version. Restriction to very thin shells, due to the fact that through-the-thickness propagation is not accounted for, and lack of the possibility to model delamination in layered composites are among the most important. Furthermore, as expected, the discrete release of fracture energy upon crack propagation along element sides produces significant, unphysical stress oscillations which can pollute the results. Possible improvements are under study also for this problem.

Acknowledgments

The financial support by Tetra Pak Carton Ambient is kindly acknowledged.

References

AbuBakar, A., Dow, R.. Simulation of ship grounding damage using the finite element method. International Journal of Solids and Structures 2013;50:623–636.

Ahmed, A., van der Meer, F.P., Sluys, L.J.. A geometrically nonlinear discontinuous solid-like shell element (DSLS) for thin shell structures. Computer Methods in Applied Mechanics and Engineering 2012;201-204:191–207.

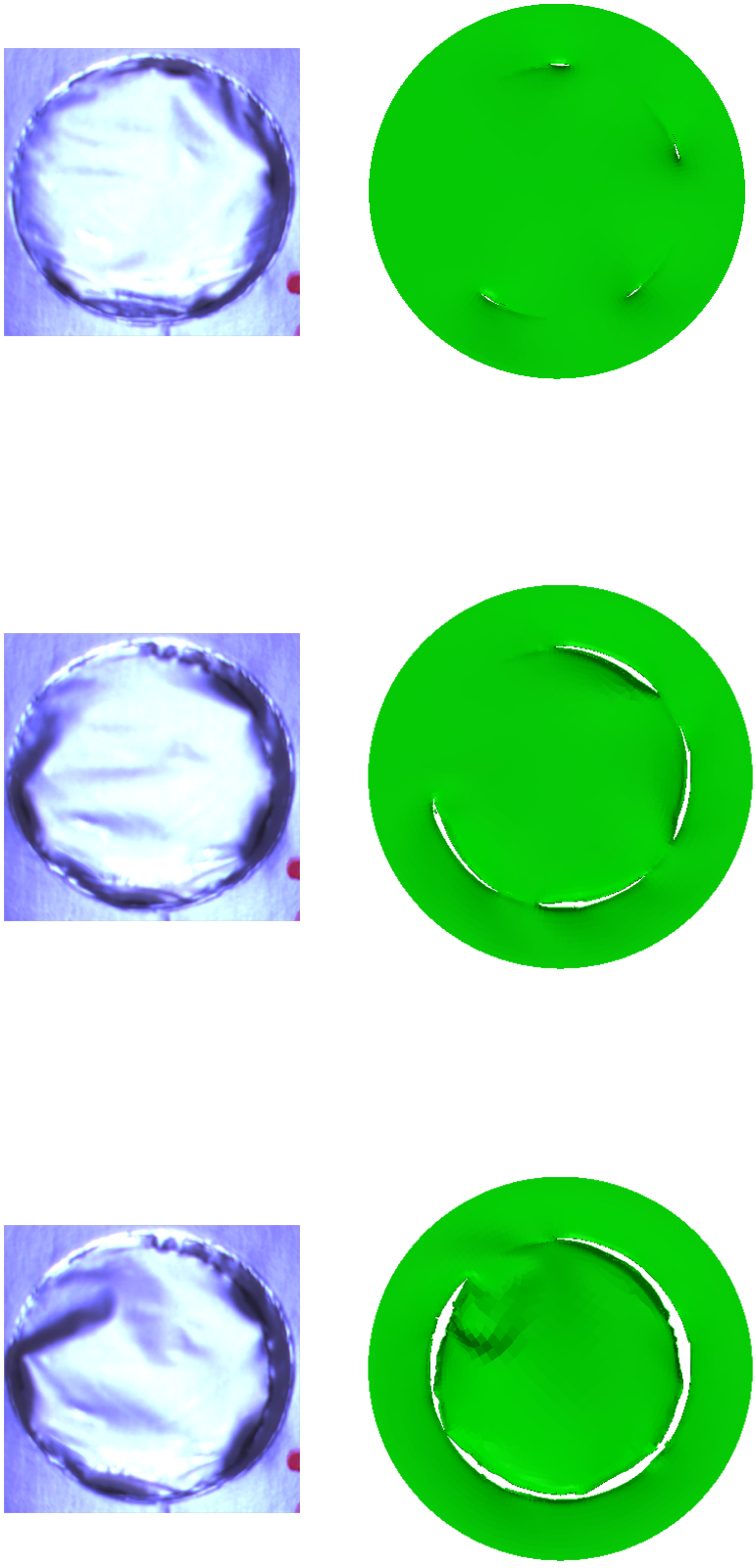

Figure 29: Cap opening. Comparison of crack propagation patterns in experiments (left) and numerical simulation (right), at synchronized time instants.

Areias, P.M.A., Belytschko, T.. Non-linear analysis of shells with arbitrary evolving cracks using XFEM. International Journal for Numerical Methods in Engineering 2005;62(3):384–415.

Areias, P.M.A., Song, J.H., Belytschko, T.. Analysis of fracture in thin shells by overlapping paired elements 2006;195:5343–5360.

Atkins, A.. Note on scaling in rigid-plastic fracture mechanics. International Journal of Mechanical Sciences 1990;32:547–548.

Atkins, A.. Letter to the Editor. International Journal of Mechanical Sciences 1991;33:69–71.

Atkins, A., Xu, X.. Slicing of soft flexible solids with industrial applications. International Journal of Mechanical Sciences 2005;47:479–492.

Atkins, T.. The science and engineering of cutting. Oxford, UK, 2009.

Bathe, K., Dvorkin, E.. A Four-Node Plate Bending Element Based on Mindlin-Reissner Plate Theory and a Mixed Interpolation. International Journal for Numerical Methods in Engineering 1985;21:367–383.

Beltman, W., Shepherd, J.. Linear Elastic Response of Tubes To Internal Detonation Loading. Journal of Sound and Vibration 2002;252:617–655.

Belytschko, T., Lin, J., Tsay, C.. Explicit algorithms for the nonlinear dynamics of shells. Computer Methods in Applied Mechanics and Engineering 1984;42:225–251.

Caleyron, F., Combescure, A., Faucher, V., Potapov, S.. Dynamic simulation of damage-fracture transition in smoothed particles hydrodynamics shells. Int J Numer Meth Engng 2012;90(6):707–738.

Chao, T., Shepherd, J.. Fracture response of externally flawed aluminum cylindrical shells under internal gaseous detonation loading. International Journal of Fracture 2005;134:59–90.

Cirak, F., Ortiz, M., Pandolfi, A.. A cohesive approach to thin-shell fracture and fragmentation. Computer Methods in Applied Mechanics and Engineering 2005;194:2604–2618.

Cocchetti, G., Pagani, M., Perego, U.. Selective mass scaling and critical time-step estimate for explicit dynamics analyses with solid-shell elements. Computers & Structures 2012;.

Comi, C., Mariani, S., Negri, M., Perego, U.. A one-dimensional variational formulation for quasibrittle fracture. Journal of Mechanics of Material and Structures 2006;1:1323–1343.

Do, B.C., Liu, W., Yang, Q.D., Su, X.Y.. Improved cohesive stress integration schemes for cohesive zone elements. Engineering Fracture Mechanics 2013;.

Fagerström, M., Larsson, R.. Theory and numerics for finite deformation fracture modelling using strong discontinuities. Int J Numer Meth Engng 2006;66(6):911–948.

Frangi, A., Pagani, M., Perego, U., Borsari, R.. Directional cohesive elements for the simulation of blade cutting of thin shells. Computer Modeling in Engineering & Sciences 2010;57(3):205–224.

Giampieri, A., Perego, U.. An interface finite element for the simulation of localized membrane-bending deformation in shells. Computer Methods in Applied Mechanics and Engineering 2011;200:2378–2396.

Hansbo, A., Hansbo, P.. A finite element method for the simulation of strong and weak discontinuities in solid mechanics. Computer Methods in Applied Mechanics and Engineering 2004;193(33-35):3523–3540.

Hauptmann, R., Schweizerhof, A.. A systematic development of 'solid-shell' element formulations for linear and non-linear analyses employing only displacement degrees of freedom. International Journal for Numerical Methods in Engineering 1998;42:49–69.

Holzapfel, G.. Nonlinear solid mechanics: a continuum approach for engineering. John Wiley, 2000.

Jones, N., Jouri, W.. A study of plate tearing for ship collision and grounding damage. J Ship Research 1987;31(4):273–288.

Lake, G., Yeoh, O.. Measurement of rubber cutting resistance on the absence of friction. International Journal of Fracture 1978;14:509–526.

Larsson, R., Mediavilla, J., Fagerström, M.. Dynamic fracture modeling in shell structures based on XFEM. Int J Numer Meth Engng 2011;86(4-5):499–527.

Lee, H., Parks, D.. Line-spring finite element for fully plastic crack growth-ii. surface-cracked plates and pipes. International Journal of Solids and Structures 1998;35(36):5139–5158.

Li, W., Siegmund, T.. An analysis of crack growth in thin-sheet metal via a cohesive zone model. Engineering Fracture Mechanics 2002;69:2073–2093.

Lu, G., Calladine, C.. On the cutting of a plate by a wedge. International Journal of Mechanical Sciences 1990;32:293–313.

Mariani, S., Perego, U.. Extended finite element method for quasi-brittle fracture. Int J Numer Meth Engng 2003;58(1):103–126.

Menouillard, T., Belytschko, T.. Smoothed nodal forces for improved dynamic crack propagation modeling in XFEM. Int J Numer Meth Engng 2010;84(1):47–72.

Moës, N., Belytschko, T.. Extended finite element method for cohesive crack growth. Engineering Fracture Mechanics 2002;69(7):813–833.

Moës, N., Dolbow, J., Belytschko, T.. A finite element method for crack growth without remeshing. International Journal for Numerical Methods in Engineering 1999;46:131–150.

Mostofizadeh, S., Fagerström, M., Larsson, R.. Dynamic crack propagation in elastoplastic thin-walled structures: Modeling and validation. Int J Numer Meth Engng 2013;96(2):63–86.

Muscat-Fenech, C., Atkins, A.. Denting and fracture of sheet steel by blunt and sharp obstacles in glancing collisions. International Journal of Impact Engineering 1998;21:499–519.

Pagani, M., Reese, S., Perego, U.. Computationally efficient explicit nonlinear analyses using reduced integration-based solid-shell finite elements. Computer Methods in Applied Mechanics and Engineering 2013;.

Pandolfi, A., Ortiz, M.. An eigenerosion approach to brittle fracture. Int J Numer Meth Engng 2012;92(8):694–714.

Papoulia, K., San, C., Vavasis, S.. Time continuity in cohesive finite element modeling. International Journal for Numerical Methods in Engineering 2003;58:679–701.

Ren, B., Li, S.. Modeling and simulation of large-scale ductile fracture in plates and shells. International Journal of Solids and Structures 2012;49:2373–2393.

Rice, J.R., Levy, N.. The part-through surface crack in an elastic plate. Journal of Applied Mechanics 1972;39(1):185–194.

Schwarze, M., Reese, S.. A reduced integration solid-shell finite element based on the EAS and the ANS concept–Large deformation problems. International Journal for Numerical Methods in Engineering 2011;85:289–329.

Simo, J., Miehe, C.. Associative coupled thermoplasticity at finite strains: Formulation, numerical analysis and implementation. Computer Methods in Applied Mechanics and Engineering 1992;98:41–104.

Simonsen, B.C., Törnqvist, R.. Experimental and numerical modelling of ductile crack propagation in large-scale shell structures. Marine Structures 2004;17:1–27.

Simonsen, B.C., Wierzbicki, T.. Plasticity, fracture and friction in steady-state plate cutting. Internation Journal of Impact Engineering 1998;21:387–411.

Song, J.H., Belytschko, T.. Dynamic Fracture of Shells Subjected to Impulsive Loads. Journal of Applied Mechanics 2009;76:051301.

Vossen, B., Schreurs, P.J.G., van der Sluis, O., Geers, M.G.D.. On the lack of rotational equilibrium in cohesive zone elements. Computer Methods in Applied Mechanics and Engineering 2013;254:146–153.

Wells, G.N., de Borst, R., Sluys, L.J.. A consistent geometrically non-linear approach for delamination. Int J Numer Meth Engng 2002;54(9):1333–1355.

Wierzbicki, T., Bao, Y., Lee, Y.W., Bai, Y.. Calibration and evaluation of seven fracture models. International Journal of

Mechanical Sciences 2005;47:719–743.

Wierzbicki, T., Thomas, P.. Closed-form solution for wedge cutting force through thin metal sheets. International Journal of Mechanical Sciences 1993;35:209–229.

Zavattieri, P.. Modeling of crack propagation in thin-walled structures using a cohesive model for shell elements. Journal fo Applied Mechanics 2006;73:948–958.

Zheng, Z., Wierzbicki, T.. A theoretical study of steady-state wedge cutting through metal plates. International Journal of Fracture 1996;78:45–66.